Multiple time-scales of decision making in the hippocampus and prefrontal cortex

Authors: Wenbo Tang[1,3], Justin D. Shin[1,3] and Shantanu P. Jadhav[1,2,*]

Affiliations:

[1]Graduate Program in Neuroscience, Brandeis University, Waltham, MA, 02453, USA.

[2]Neuroscience Program, Department of Psychology, and Volen National Center for Complex Systems, Brandeis University, Waltham, MA, 02453, USA.

[3]These authors contributed equally to this work

*Correspondence to: shantanu@brandeis.edu

ABSTRACT

The prefrontal cortex and hippocampus are crucial for memory-guided decision-making. Neural activity in the hippocampus exhibits place-cell sequences at multiple timescales, including slow behavioral sequences (~seconds) and fast theta sequences (~100-200 ms) within theta oscillation cycles. How prefrontal ensembles interact with hippocampal sequences to support decision-making is unclear. Here, we examined simultaneous hippocampal and prefrontal ensemble activity during learning of a spatial working-memory decision task. We found clear theta sequences in prefrontal cortex, nested within its behavioral sequences. In both regions, behavioral sequences maintained representations of current goals during navigation. In contrast, hippocampal theta sequences encoded alternatives for deliberation, and were coordinated with prefrontal theta sequences that predicted upcoming choices. During error trials, these representations were preserved to guide ongoing behavior, whereas replay sequences during inter-trial periods were impaired prior to navigation. These results establish cooperative interaction between hippocampal and prefrontal sequences at multiple timescales for memory-guided decision making.

KEYWORDS

Hippocampus; Prefrontal cortex; Decision making; Working memory; Spatial learning; Sequence; Replay; Sharp-wave ripple; Theta oscillation; Planning.

INTRODUCTION

The neural substrates that support decision making are still not fully understood. The link between decision making and neural representations at the behavioral timescale has been studied extensively in various cortical and sub-cortical circuits of different species. Early classic work showed that during tasks involving sustained attention or decision making, neurons in the prefrontal cortex (PFC) and the posterior parietal cortex (PPC) can exhibit persistent activity over seconds throughout retention intervals for maintenance of decision-related information (Fuster, 2015; Goldman-Rakic, 1995; Miller et al., 2018; Sreenivasan and D'Esposito, 2019). In contrast to these low-dimensional representations that require long-lived stable states, decision-related information can also be held in a dynamic population code. At the ensemble level, heterogenous activity patterns comprising sequences of neuronal activation that span entire task periods have emerged as a common coding scheme in many brain regions, including PFC (Baeg et al., 2003; Fujisawa et al., 2008; Ito et al., 2015), hippocampus (Ito et al., 2015; Pastalkova et al., 2008), PPC (Crowe et al., 2010; Harvey et al., 2012) and striatum (Bakhurin et al., 2016; Barnes et al., 2005).

In addition to this behavioral-timescale activity, recent work has raised the possibility that neural dynamics at fast, cognitive timescales that occur transiently during discrete subsets of task periods can also underlie upcoming decisions. In many brain areas, such as prefrontal, parietal, orbitofrontal cortices, and hippocampus, population activity can change in an abrupt, coordinated, and transient manner in support of flexible decisions (Bernacchia et al., 2011; Durstewitz et al., 2010; Johnson and Redish, 2007; Karlsson et al., 2012; Latimer et al., 2015; Lundqvist et al., 2016; Rich and Wallis, 2016). For example, discrete transient bursts of gamma and beta oscillations in PFC have been shown to increase with working-memory load during delays (Lundqvist et al., 2016). In particular, recent studies have identified time-compressed neuronal

sequences in the hippocampus as a specific cell-assembly pattern at fast timescales that can support decision-making processes.

Hippocampal theta sequences provide time-compressed ensemble representations of spatial paths within single cycles of theta oscillations (6-12 Hz) during active navigation, which reflect a candidate neural mechanism for planning at decision time (Johnson and Redish, 2007; Kay et al., 2020; Papale et al., 2016; Pezzulo et al., 2019; Zheng et al., 2020; Zielinski et al., 2020). Whether theta sequences exist in PFC during decision-making has yet to be determined. Further, during pauses in exploration, replay sequences are observed in the hippocampus during individual sharp-wave ripples (SWRs; Carr et al. 2011), and are known to interact with PFC to reactivate past and future trajectories on the temporal scale of 100-200 ms during memory-guided decisions (Shin et al., 2019; Tang and Jadhav, 2019). Disruption of fast sequences in the hippocampus, while leaving behavioral-timescale spatial representations intact, can impair navigation decisions (Fernandez-Ruiz et al., 2019; Jadhav et al., 2012; Petersen and Buzsaki, 2020; Robbe and Buzsaki, 2009). Thus, fast hippocampal sequences are promising transient activity patterns that can support decision making at sub-second speed (Buzsaki et al., 2014; Kay et al., 2020; Papale et al., 2016; Pezzulo et al., 2019; Shin et al., 2019). Whether and how these fast-timescale representations are organized together in hippocampal-prefrontal circuits, and how they, especially theta sequences, are linked to behavioral-timescale mechanisms for decision making is unknown. To address these questions, we examined neuronal ensemble activity simultaneously in the hippocampus and PFC of rats during learning of a spatial working-memory decision task.

RESULTS

Choice-specific neuronal sequences in CA1 and PFC during navigation decisions

We trained nine rats to learn a spatial working-memory task (**Figure 1A**). In this delayed alternation task, animals had to traverse a delay section (i.e., “center stem”) of a W-maze on each trial, and the critical memory demand of this task is to distinguish left (L) versus right (R) choices (**Figure 1A**): when the animals return inward from the side arm to the center reward well, they are required to remember their past choice between two possible locations (L vs. R arm; inbound reference-memory trial, **Figure 1A**, *left*); and have to choose the opposite side arm correctly for reward after running outward through the stem when facing the two upcoming options (outbound working-memory trial, **Figure 1A**, *right*) (Jadhav et al., 2012; Kim and Frank, 2009). This task is known to require both the hippocampus and PFC for learning (Fernandez-Ruiz et al., 2019; Jadhav et al., 2012; Kim and Frank, 2009; Maharjan et al., 2018), and involves memory-guided decision making (Jadhav et al., 2016; Shin et al., 2019; Yu and Frank, 2015). All subjects learned the task rules over eight training sessions (or epochs; 15-20 mins per sessions) in a single day, and performed with high levels of accuracy at the end of the training (**Figure 1B**; final performance: 92.5 ± 1.8% for inbound, 80.8 ± 2.8% for outbound, in mean ± SEM).

We used continuous and simultaneous recordings from ensembles of dorsal CA1 hippocampal and PFC neurons as rats learned this task (**Figures 1C** and **S1**; mean ± SEM = 43.9 ± 7.6 CA1 place cells, 29.8 ± 5.6 PFC cells per session). As a result of spatially specific firing, sequences of CA1 and PFC cells successively activated on the timescale of seconds as the rat ran through a trajectory (i.e., behavioral sequences), as previously reported by several groups (Frank et al., 2000; Fujisawa et al., 2008; Ito et al., 2015; Shin et al., 2019; Wood et al., 2000). Further, these sequences were reactivated on the timescale of hundreds of milliseconds during SWRs at the reward well (i.e., replay sequences**; Figure 1C**), confirming our previous findings (Shin et al., 2019). Notably, within each cycle of theta oscillations during navigation, which corresponds to expression of fast CA1 theta sequences (Dragoi and Buzsaki, 2006; Foster and Wilson, 2007; Gupta et al., 2012; Skaggs et al., 1996), we found that PFC cells were organized

into sequences as well, and could occur concurrently with the hippocampal sequences (**Figure 1C**). Given these observations, we further quantified these sequences and investigated their roles in decision making.

First, we characterized how CA1 and PFC neurons encode choices on the behavioral timescale. We found that at the single-cell level, many CA1 and PFC cells exhibited strong preferential firing during navigation on L- versus R- side trajectory (trajectory-selective cells; mean ± SEM = 38.4 ± 1.2% in CA1, 23.5 ± 1.3% in PFC for inbound, 35.0 ± 0.7% in CA1, 20.9 ± 0.6% in PFC for outbound; **Figures 1D** and **1E**), consistent with prior reports (Frank et al., 2000; Fujisawa et al., 2008; Ito et al., 2015; Shin et al., 2019; Wood et al., 2000). These trajectory-selective cells, when ordered by the peak firing on the preferred trajectory, form unique sequences for each choice type spanning the entire trial length at the behavioral timescale, including the common center stem prior to the choice point (CP) and the side arms after the CP (**Figures 1F** and **1G**).

To directly assess the cell-assembly representation of the animals' choices, we used a memoryless Bayesian decoding algorithm (see **METHODS**) (Shin et al., 2019). We found that behavioral sequences in CA1 and PFC consistently predicted the animals' current location and choice well above chance level across all positions of a trial (Fujisawa et al., 2008; Ito et al., 2015; Shin et al., 2019; Wood et al., 2000), even on the common center stem (**Figures 1H** and **1I** and **S1**). Notably, the decoding accuracy on the center stem significantly increased in CA1 (p = 0.0003 and < 1e-4 for outbound and inbound, respectively), and was stable in PFC across sessions (*p's* > 0.05 for outbound and inbound, Kruskal-Wallis test with Dunn's *post hoc*; **Figures 1H** and **1I,** *right*), in agreement with our previous findings of an increased proportion of CA1 "splitter cells" (center-stem trajectory-selective cells) and a stable proportion of PFC "splitter cells" over learning (Shin et al., 2019). In addition, the larger proportions of inbound splitter cells (Shin et al., 2019) also contributed to better decoding for inbound choices compared to that for outbound (**Figures**

128 **1H** and **1I**). Nonetheless, behavioral sequences of CA1 and PFC cells represented unique choice
129 types throughout the course of learning.

130 Therefore, these results suggest that choice information progresses through
131 heterogeneous neuronal sequences in CA1 and PFC at the behavioral timescale as rats run along
132 each trajectory. Importantly, these choice representations also provide distinguishable templates
133 for the Bayesian decoder to identify and determine the content of fast theta sequences.

134

135 **Fast theta sequences in CA1 and PFC**

136 Theta oscillations are prominent in CA1 during navigation, and CA1 cell assemblies are organized
137 into theta sequences within single oscillation cycles. While it is not known whether ordered
138 sequences of PFC cells occur during hippocampal theta oscillations, previous studies have shown
139 that PFC cells phase-lock and phase-precess (i.e., spikes of a cell occur at progressively earlier
140 theta phases as an animal move through its spatial field) to hippocampal theta oscillations
141 (Jadhav et al., 2016; Jones and Wilson, 2005a; Siapas et al., 2005; Sigurdsson et al., 2010);
142 further, theta-frequency synchrony and coherent spatial coding between the hippocampus and
143 PFC is prominent during memory-guided navigation (Benchenane et al., 2010; Gordon, 2011;
144 Hasz and Redish, 2020; Jones and Wilson, 2005b; Sigurdsson et al., 2010; Zielinski et al., 2019).

145 In order to statistically identify theta sequences in CA1 and PFC, population spikes within
146 each candidate hippocampal theta cycle (≥ 5 cells active in a given brain region) during active
147 running were analyzed using the Bayesian decoding approach, and the sequential structure of
148 the Bayesian reconstructed positions was evaluated by shuffling procedures (see **METHODS**).
149 Using this method, clear theta sequences were found in CA1 during inbound and outbound
150 navigation across all sessions (**Figures 2A-2C**), Intriguingly, significant theta sequences were
151 also detected in PFC (**Figures 2D-2F**). The prevalence of theta sequences in PFC was similar to

that in CA1 (**Figure 2G**), although as expected, higher trajectory scores (suggesting more reliable timing of sequences) were observed in CA1 compared to PFC (**Figure 2H**). Furthermore, the trajectory scores and slopes (sequence speed) in both regions increased over learning (**Figures 2H** and **2I**). Finally, consistent with previous studies in CA1 (Gupta et al., 2012; Wikenheiser and Redish, 2015; Zheng et al., 2016), the majority of CA1 (~70%) and PFC (~60%) theta sequences successively represented past, present, and future locations within each theta cycle (i.e., forward sequences; **Figures 2J** and **S2A-S2C**), at a velocity approximately 4-15 times faster than an animal's true running speed (**Figure 2I**). These properties of CA1 and PFC theta sequences were replicated with a 10-cell threshold and different shuffling procedures (**Figure S2**), suggesting that the observation of theta sequences in CA1 and PFC was not a trivial result of our decoding methodology.

Look-ahead of theta sequences during outbound versus inbound navigation

Prior work has shown that hippocampal forward theta sequences encode paths ahead of the animal, potentially providing a "look-ahead" prediction of upcoming locations (Dragoi and Buzsaki, 2006; Foster and Wilson, 2007; Gupta et al., 2012; Lisman and Redish, 2009; Maurer and McNaughton, 2007; Skaggs et al., 1996; Wikenheiser and Redish, 2015). To investigate how these theta sequences related to animals' memory state and upcoming behavior, we examined the Bayesian reconstructed positions of forward-shifted candidate theta sequences in different theta-phase bins during reference-memory-guided inbound versus working-memory-guided outbound navigation. We found that the positions behind the actual location of the animal were decoded with higher probability during inbound than outbound navigation in both CA1 and PFC, (**Figures 3A-3D**), implying that inbound sequences started farther behind and outbound sequences sweep father ahead of the current animal position. To further confirm this result, we directly compared the start and end positions of each significant theta sequence, and indeed,

forward sequences in both CA1 and PFC started farther behind the actual position of the animal during inbound navigation, whereas they ended farther ahead of the animal during outbound navigation (**Figures 3E** and **3F**). A possibility that could bias this look-ahead difference is that the choice point may represent an attractor network, 'pulling' representations toward it. This hypothesis would predict a stronger effect when an animal approaches the choice point compared to the reward well. However, we obtained similar results in these two situations (**Figure S3**), indicating the difference in theta-sequence look-ahead is not a simple result of the attractor behavioral states of the choice point or reward well.

We then investigated potential neuronal mechanisms underlying this shift in ahead-sequence length. On a single-cell level, previous theoretical and experimental evidence has suggested that the initial tail of asymmetric spatial fields allows cells with fields ahead of an animal's position to fire during earlier theta cycles, which results in "look-ahead" of theta sequences (Burgess and O'Keefe, 2011; Mehta et al., 2002; Mehta et al., 2000; Skaggs et al., 1996; Wikenheiser and Redish, 2015). We therefore examined the relationship between firing field asymmetry and the shift in ahead-sequence length during outbound and inbound navigation (**Figures 4A-4D**). We found that while the asymmetry developed with experience, as reported previously in CA1 (**Figures 4A-4C**) (Mehta et al., 2000), working-memory-guided outbound navigation was associated with fields with a more extended initial tail compared to inbound travel for both CA1 and PFC (**Figures 4A-4C**). This effect was also stronger for trajectory-selective than non-selective cells in both regions (**Figure 4D**).

Further, a prominent model suggests that phase precession of individual neurons may give rise to the look-ahead forward sweep of theta sequences in CA1 (Dragoi and Buzsaki, 2006; Skaggs et al., 1996). We therefore examined if the shift in ahead-sequence length was a consequence of change in phase precession speed during inbound versus outbound navigation. Consistent with previous studies (Jones and Wilson, 2005a; Skaggs et al., 1996), we found CA1

202 and PFC cells phase-precessing to hippocampal theta oscillations (**Figures 4E** and **4F**). However,
203 similar slopes of theta phase precession were observed for inbound and outbound navigation in
204 both regions (**Figures 4G** and **4H**), which therefore cannot simply explain the difference in
205 inbound and outbound look-ahead of theta sequences.

206 Together, these results suggest that beyond the pure sensory features of the environment,
207 memory demands influenced the look-ahead properties of theta sequences in both CA1 and PFC,
208 and the increased look-ahead distance during working-memory-guided outbound navigation
209 allows the animal to represent future locations earlier in the trajectory, which can aid in decision
210 making.

211

212 **Theta sequences support vicarious memory recall**

213 How do CA1 and PFC theta sequences relate to the animals' upcoming choices when multiple
214 options are available, and do they encode current goal throughout navigation similar to the
215 behavioral sequences (**Figure 1**)? Prior work has reported that hippocampal population activity
216 at the theta timescale can represent alternatives, which potentially supports deliberation (Johnson
217 and Redish, 2007; Kay et al., 2020), and such a population code is linked to single-cell cycle
218 skipping, in which cells fire on alternate theta cycles (Kay et al., 2020). Therefore, we first
219 examined single-cell firing at the theta timescale in CA1 and PFC. Consistent with previous
220 studies (Dragoi and Buzsaki, 2006; Kay et al., 2020), we observed normal theta rhythmic (i.e.,
221 non-skipping; firing on adjacent cycles) and cycle skipping (i.e., firing on every other cycle) cells
222 in CA1 (**Figures 5A** and **5B**). Intriguingly, we found that a large proportion of theta-modulated
223 cells in PFC also fired in regular alternation during hippocampal theta oscillations (i.e., cycle
224 skipping; Inbound: 53.4%, 95 out of 178; outbound: 49.7%, 91 out of 183; **Figures 5C** and **5D**).

225 Given the single-cell property of cycle-skipping identified above in both regions, we next
226 examined how populations of CA1 and PFC cells encoded choices during theta sequences.

227 Indeed, we found that CA1 theta sequences can encode alternatives (**Figure 6A**), as previously
228 reported (Johnson and Redish, 2007; Kay et al., 2020). However, when we examined the
229 representations of choices by theta sequences along each trajectory, we found these
230 representations were distinct in CA1 and PFC during decision-making periods prior to the choice
231 point (CP). Before the CP (corresponding to periods on the center stem for outbound navigation;
232 **Figure 6B**), CA1 theta sequences serially encoded both alternative trajectories (**Figures 6C** and
233 **6G** and **S4-S5**). In contrast, PFC theta sequences preferentially encoded the animal's current
234 choice (**Figures 6E** and **6G** and **S4-S5**). After the choice was made (i.e., after CP; **Figure 6B**),
235 as expected, both CA1 and PFC theta sequences preferentially encoded the animal's current
236 choice as the animal's ran down the track toward reward (**Figures 6D** and **6F** and **6G** and **S4-**
237 **S5**). Note that after CP, CA1 theta sequences representing the alternative choice only constituted
238 a minority of the total sequences, reminiscent of the previously findings of a small proportion of
239 hippocampal theta sequences representing the alternative running direction on a linear track
240 (Feng et al., 2015; Wang et al., 2020), and encoding locations far away from an animal's current
241 position (Gupta et al., 2012; Wikenheiser and Redish, 2015).

242 The choice representations of theta sequences were robust across sessions (**Figure 6G**),
243 enabling trial-by-trial prediction of decisions, in which upcoming choice was decoded by PFC theta
244 sequences well above chance before the CP, whereas CA1 theta sequences encoded actual and
245 alternative available paths equivalently before the CP (**Figures 6H** and **6I**). Similar results were
246 found for inbound trials (**Figures S4-S5**). Note that these results cannot be accounted for by
247 similar spatial-field templates for L versus R choices on the center stem, because spatial-field
248 activity can decode L versus R choices well above chance within the center stem in both CA1 and
249 PFC, and this decoding accuracy was in fact higher for CA1 than PFC (**Figures 1H** and **1I**).
250 Furthermore, similar effects were found after controlling for different shuffling procedures (**Figure**
251 **S5A**) and examining the last theta sequence on the center stem (**Figure S5D**).

Next, we asked if PFC theta sequences encoded choices that were coherent with CA1 sequences within single theta cycles. We detected PFC theta sequences simultaneously with CA1 theta sequences for a subset of theta cycles (**Figures 6J** and **6K**; mean ± SEM = 10.53 ± 1.42%, and 11.17 ± 1.52% out of significant sequences for outbound and inbound, respectively; $p = 0.78$ comparing outbound vs. inbound proportions, rank-sum test). Among these synchronous sequence events, when CA1 theta sequences represented the actual choice, PFC sequences were also significantly biased to the actual choice, whereas this coherent CA1-PFC representation was not observed when CA1 theta sequences represented the alternative choice (**Figure 6L**).

Taken together, these results suggest that CA1-PFC theta sequences occurred in tandem with, but distinct from, behavioral sequences for choice representations, and that CA1-PFC theta sequences underlie a novel mechanism that supports vicarious memory recall on a fast timescale for deliberative decision making.

CA1 and PFC sequences during incorrect trials

While we found a clear relationship between CA1 and PFC sequences at both behavioral and theta timescales for upcoming decisions, it remained unclear if these contributed to correct versus erroneous decisions. We therefore analyzed neural activity during correct versus incorrect trials, with incorrect trials corresponding to erroneous outbound navigation to the same side arm as the past inbound visit (**Figure 7A**). We found that sequential firing that occurred at the behavioral timescale during incorrect trials was similar to that during correct trials (**Figure 7B**), and the decoding accuracy for the chosen side was comparable for correct and incorrect trials (**Figure 7C**; inbound trials for the incorrect condition were considered as the one right before an incorrect outbound trial). Furthermore, CA1 and PFC theta-sequence prediction of upcoming choice was also similar for correct and incorrect trials (**Figure 7D**).

Correct versus incorrect trials did not differ in running speed and theta power (**Figures S6A** and **S6B**). CA1-PFC theta coherence and the strength of single-cell phase-locking to theta oscillations during navigation, which have been proposed to support spatial working memory (Benchenane et al., 2010; Gordon, 2011; Jones and Wilson, 2005b; Sigurdsson et al., 2010), were also similar between correct versus incorrect trials (**Figures S6C-S6L**). Therefore, both theta-linked phenomena at the two timescales likely represented maintenance mechanisms for working memory and decision making, making it plausible that incorrect destinations were chosen prior to embarking on trajectories from the center well.

We therefore examined replay sequences during SWRs in the inter-trial periods prior to trajectory onset (**Figure 1C**). Previously, we have reported that CA1 replay sequences, similar to its theta sequences reported here, underlie deliberation between actual and alternative choices, whereas CA1-PFC reactivation represents actual choice for current trials (Shin et al., 2019). Here, we confirmed these observations (**Figures S7A-S7D**). Importantly, in addition, using CA1-PFC reactivation strength for actual versus alternative choices preceding the correct and incorrect trials (see **METHODS**), we could predict correct and incorrect responses significantly better than chance (**Figures S7E** and **S7F**), indicating impaired CA1-PFC reactivation prior to incorrect outbound navigation. These results suggest that CA1-PFC replay sequences during awake SWRs prime initial navigation decisions, which are further maintained by theta-sequence and trajectory-selective mechanisms during retention periods on a trial-by-trial basis, underlying successful performance in the working memory task.

DISCUSSION

Our findings provide a new framework that integrates multi-timescale mechanisms for memory-guided decision making. By establishing hippocampal-prefrontal population coding at different timescales, we demonstrate that two forms of cell-assembly dynamics for decision making can

be distinguished, i.e., slow behavioral-timescale sequences and fast cognitive-timescale sequences. This further enabled us to dissect the role of neuronal sequences at these different timescales in a spatial working-memory and navigation task.

First, during delay periods of the spatial navigation task on the center stem, choice information was maintained by behavioral-timescale sequences in CA1 and PFC on correct as well as incorrect trials. These sequences are contextually modulated by current journeys and goals, and can enable choice-related information processing on a behavioral timescale for planning actions (Harvey et al., 2012; Ito et al., 2015). In addition, we determined the existence of compressed-timescale theta sequences in PFC, similar to previously described CA1 theta sequences (Dragoi and Buzsaki, 2006; Foster and Wilson, 2007; Kay et al., 2020; Skaggs et al., 1996). These transient theta sequences in CA1 and PFC were nested within behavioral-timescale sequences during navigation. However, in contrast to trajectory-dependent firing sequences at the behavioral-timescale, theta sequences retain representations of choice options to support vicarious memory recall and deliberative decision making, and function in a complementary manner with fast replay sequences involved in decision priming prior to onset of navigation, highlighting novel roles of these compressed sequences in guiding ongoing choice behavior. Notably, the mechanism of using internally generated sequences to simulate future scenarios has been used as a key feature that improves performance of model-based learning computations (Daw and Dayan, 2014; Mattar and Daw, 2018; Pezzulo et al., 2019; Pezzulo et al., 2014).

At the level of single theta cycles, we found that prior to the decision-making point in the navigation task, CA1 theta sequences report both actual and alternative choices, and are unable to predict chosen destination till after the decision has been made. On the other hand, we found robust PFC theta sequences that maintain prediction of upcoming choice prior to the decision point. Thus, theta sequences underlie a cognitive timescale mechanism that also maintains choice information, with the key distinction that this fast timescale mechanism can support vicarious memory recall of different choices, which was not seen at the behavioral timescale. This

process may be important in the event that animals have to change decisions or adapt to change in contingencies (Buzsaki et al., 2014; Rich and Wallis, 2016; Yu and Frank, 2015). In agreement with this idea, a recent study has shown that theta timescale mechanisms in CA1 can not only represent possible future paths, but also possible directions of motion on a moment-to-moment basis (Kay et al., 2020). Representation of past locations within theta cycles has also been recently reported (Wang et al., 2020). Complementing these results, previous studies have shown that theta oscillation cycles comprise cognitive computation units, corresponding to segregation of cell assemblies that represent different spatial experiences (Brandon et al., 2013; Geisler et al., 2007; Gupta et al., 2012; Jezek et al., 2011) and alternatives (Johnson and Redish, 2007; Kay et al., 2020; Papale et al., 2016). The results shown here establish that the representation of alternatives in the hippocampus interacts with prefrontal theta sequences in a content-specific manner, which can be used to guide actual choices.

The exact mechanism underlying these interactions, however, remains unclear. It has been shown that cortical neurons are sensitive to temporally organized inputs from the hippocampus (Branco et al., 2010; Siapas et al., 2005; Sigurdsson et al., 2010), and pharmacological disruption of prefrontal activity results in impaired theta sequences in the hippocampus (Schmidt et al., 2019), as well as impaired performance in the W-track task (Maharjan et al., 2018). Behavioral-state dependent prefrontal-hippocampal interactions during theta oscillations can potentially also be mediated through connections with entorhinal cortex (Fernandez-Ruiz et al., 2017), nucleus reuniens (Ito et al., 2015), or other regions (Eichenbaum, 2017) that contribute to theta generation and memory retrieval. The specific roles of these circuits will need to be further elucidated in future investigations.

Notably, both theta-associated mechanisms at the two timescales during navigation supported retention during working memory periods, but did not predict errors in decisions. Rather, we found that compressed SWR replay sequences during inter-trial periods prior to the onset of trajectories prime the decision without apparent external cue triggers, which is maintained from

354 the onset of the trajectory via behavioral and theta sequences. Previous studies have shown that
355 SWR-reactivation in the hippocampus is less coordinated prior to incorrect versus correct trials
356 (Shin et al., 2019; Singer et al., 2013), and disrupting awake SWRs leads to increase in errors in
357 the spatial working memory task (Fernandez-Ruiz et al., 2019; Jadhav et al., 2012). In addition,
358 we have previously shown a relationship between forward and reverse CA1-PFC replay with past
359 and future trajectories respectively (Shin et al., 2019). Consistent with all these prior results, our
360 current findings provide definitive evidence that coherent CA1-PFC replay of future trajectories
361 prior to navigation onset primes the chosen destination in this memory-guided decision making
362 task, and errors in CA1-PFC replay predict incorrect decisions.

363 It is important to note that the expression of behavioral- and compressed-timescale
364 sequences representing different trajectories are inextricably linked. Choice-specific
365 representations of both theta and replay sequences depend on choice encoding through trajectory
366 preferred firing of behavioral sequences. Furthermore, trajectory-selective neurons showed an
367 extended tail of their spatial fields, which is inherently a behavioral-timescale characteristic, and
368 likely contributes to trajectory-modulated look-ahead of theta sequences. Finally, there is
369 evidence that degradation of theta sequences results in impaired sequential activation during
370 sleep replay in the hippocampus (Drieu et al., 2018). Thus, it is the interactions among these
371 multi-timescale activity patterns that potentially govern decision making. The network
372 mechanisms that enable expression of sequences at distinct timescales in multiple circuits remain
373 a key question for future investigation.

374 Overall, our results provide a critical extension to classic models, which emphasize
375 behavioral-timescale activity patterns typically spanning entire retention intervals, by establishing
376 a role of discrete, fast timescale ensemble activity patterns in decision making processes. Such
377 a mechanism is broadly supported by recent findings of rapid shifts in activity patterns during
378 decision making (Bernacchia et al., 2011; Durstewitz et al., 2010; Karlsson et al., 2012; Latimer
379 et al., 2015; Rich and Wallis, 2016; Sadacca et al., 2016), including discrete gamma oscillatory

bursts in PFC underlying working memory (Lundqvist et al., 2016; Miller et al., 2018), which occur at a similar timescale to compressed theta and replay sequences. Together, these results suggest the possibility of transient LFP oscillations as informative signatures of fast evolving cell assemblies that bear on decision-making processes, and the cooperative behavioral- and cognitive-timescale mechanisms described here may reflect a general organizing principle of neural dynamics underlying decision making.

ACKNOWLEDGMENTS

This work was supported by NIH Grant R01 MH112661 and the Smith Foundation Odyssey award to S.P.J.

AUTHOR CONTRIBUTIONS

W.T., J.D.S. and S.P.J. designed the study. S.P.J. proposed and directed the project. J.D.S carried out the experiments and collected the data. W.T. analyzed the results and prepared the figures. W.T., J.D.S. and S.P.J. wrote the paper.

DECLARATION OF INTERESTS

The authors declare no conflicts of interest.

FIGURES

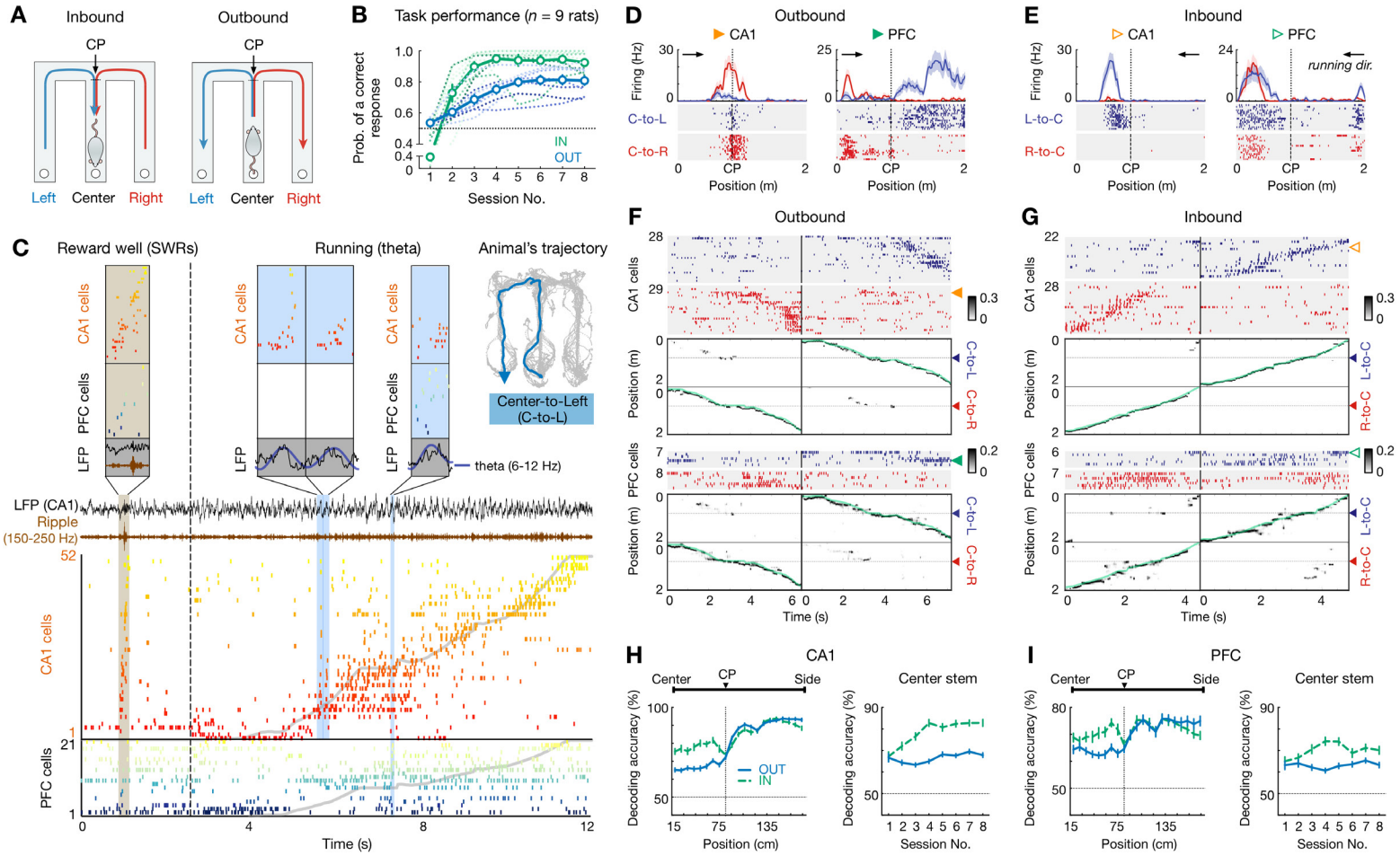

Figure 1. Choice-specific sequences in CA1 and PFC during memory-guided navigation decisions

(A) Diagrams of two possible past (inbound; *left*) and future (outbound; *right*) scenarios during a W-maze spatial alternation task. In this task, rats have to remember their past choice between two possible locations (Left vs. Right arms; *left*), and then choose the opposite arm correctly (*right*; see **METHODS**). CP: choice point.

(B) Behavioral performance of all 9 rats that learned the inbound (IN; green) and outbound (OUT; blue) components of the task over 8 sessions within a single day. Dashed lines: individual animals. Thick lines with error bars: mean with SEMs. Horizontal dashed lines: chance-level of 0.5. Prob.: probability.

(C) Simultaneously recorded ensembles of CA1 and PFC cells, forming slow behavioral sequences spanning the entire trajectory (~8 s), fast replay sequences (~260 ms; brown shading), and fast theta

sequences (~100-200 ms; blue shadings). Each row represents a cell ordered and color-coded by field center on the Center-to-Left (C-to-L) trajectory shown *top right*. Gray lines: actual position. Dashed vertical line: reward well exit. Black, brown, and dark blue lines: broadband, ripple-band, and theta-band filtered LFPs from one CA1 tetrode, respectively.

(D-I) Choice-predictive representations of behavioral sequences in CA1 and PFC.

(D and **E)** Four trajectory-selective example cells during **(D)** outbound and **(E)** inbound navigation (shadings: SEMs; black arrowheaded line indicates animal's running direction).

(F and **G)** Example choice-specific behavioral sequences. For each plot pair, the *top* illustrates a raster of trajectory-selective cell assemblies ordered by field centers on the preferred trajectory; the *bottom* shows population decoding of animal's choice and locations at the behavioral timescale (bin = 120 ms; note that summed probability of each column across two trajectory types is 1). Green and yellow arrowheads indicate the example cells shown in **(D)** and **(E)**. Color bar: posterior probability. Green lines: actual position. Blue and red arrowheads: the CP. Note that the rasters only show trajectory-selective cells, whereas the population decoding was performed using all cells recorded in a given region.

(H and **I)** Behavioral sequences in **(H)** CA1 and **(I)** PFC predicted current choices. *Left*: decoding accuracy of current choice over locations (n = 9 rats × 8 sessions); *Right*: decoding accuracy of current choice on the center stem across sessions. Note that the decoding performance is significantly better than chance (50%) over locations and sessions (all p's < 1e-4, rank-sum tests). Error bars: SEMs. OUT: outbound; IN: inbound.

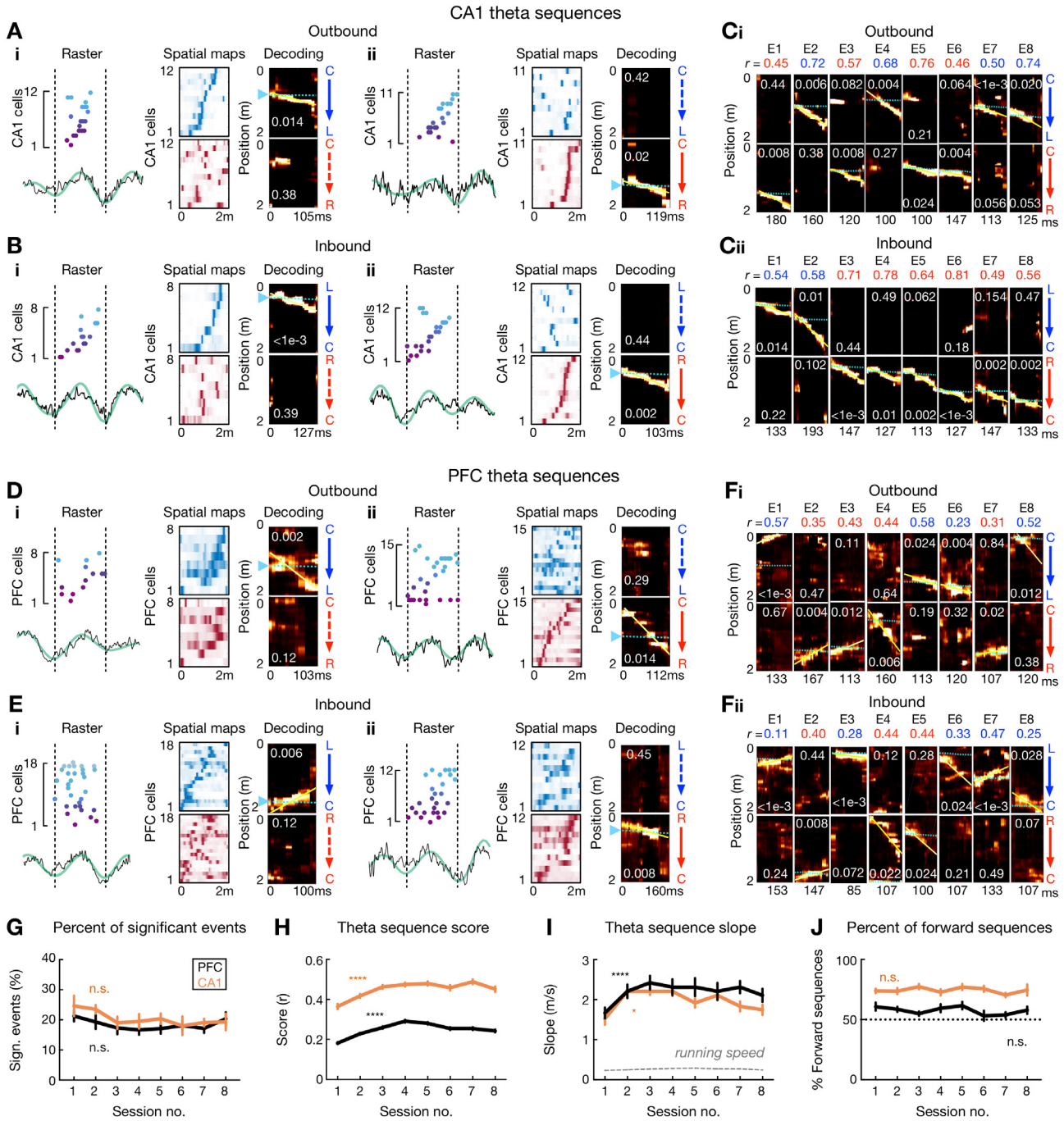

Figure 2. Theta sequences in CA1 and PFC over learning

(A and **B)** Four examples of theta sequences in CA1 for **(A)** outbound and **(B)** inbound trajectories. *Left*: spikes ordered and color coded by field center on the decoded trajectory (see *Right*) over a theta cycle. Broadband (black) and theta-band filtered (green) LFPs from CA1 reference tetrode shown below. *Middle*: corresponding linearized spatial fields (blue colormap for L-side trajectory, red colormap for R-side trajectory). *Right*: Bayesian decoding with *p*-values based on shuffled data denoted (see **METHODS**).

Yellow lines: the best linear fit on the decoded trajectory. Cyan lines and arrowheads: actual position. Note that summed probability of each column across two trajectory types is 1.

(C) Example CA1 theta sequences across 8 sessions (or epochs, E1 to E8). Each column of plots represents a theta-sequence event. Sequence score (*r*) on the decoded trajectory denoted.

(D and **E)** Four examples of theta sequences in PFC for **(D)** outbound and **(E)** inbound trajectories. Data are presented as in **(A)** and **(B)**. LFPs are from CA1 reference tetrode.

(F) Example PFC theta sequences across 8 sessions. Data are presented as in **(C)**.

(G) Percent of significant theta sequences out of all candidate sequences didn't change significantly over sessions (Session 1 vs. 8: *p's* > 0.99 for CA1 and PFC, Friedman tests with Dunn's *post hoc*). Data are presented as mean and SEM. Black line: PFC; Orange line: CA1.

(H) Theta sequence scores (*r*) improved over sessions (****p's < 1e-4 for CA1 and PFC, Kruskal-Wallis tests with Dunn's *post hoc*). Data are presented as median and SEM.

(I) Theta sequence slopes increased over sessions (*p = 0.0427 for CA1, and ****p < 1e-4 for PFC, Kruskal-Wallis tests with Dunn's *post hoc*). Dashed gray lines: mean ± SEMs of animals' running speed (small error bars may not be discernable). Data are presented as median and SEM.

(J) Percent of forward theta sequences didn't change significantly over sessions (p = 0.56 and 0.41 for CA1 and PFC, Friedman tests). Data are presented as mean and SEM.

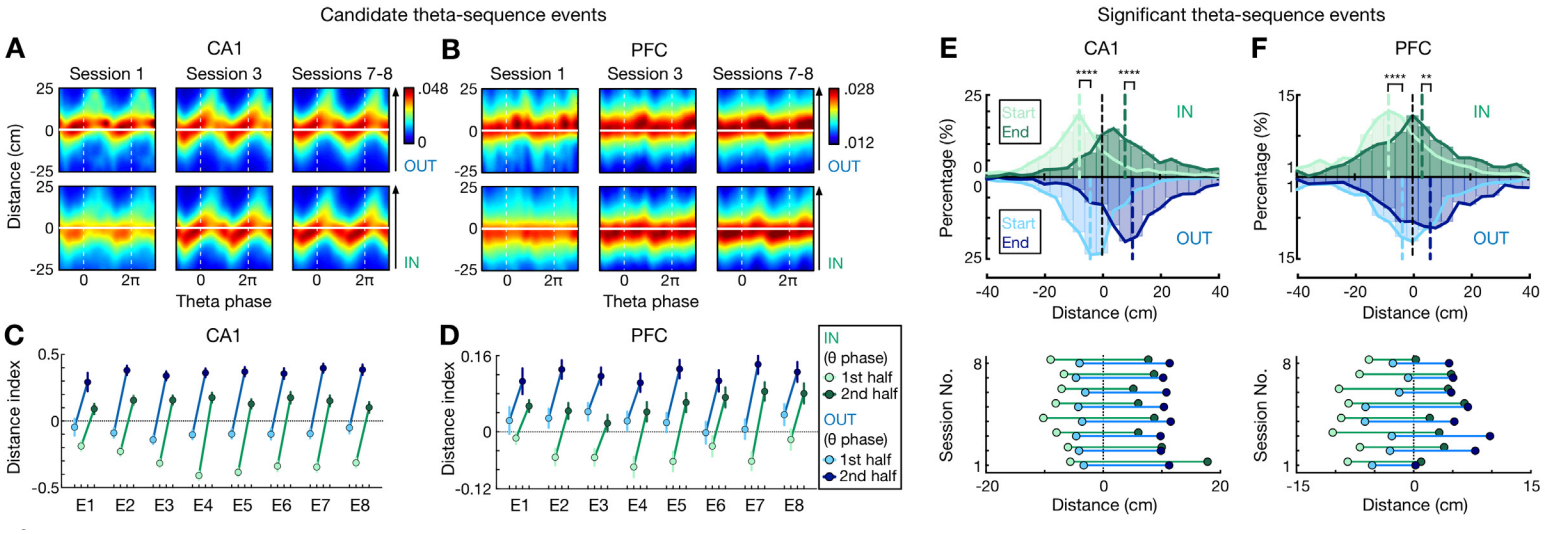

Figure 3. Look-ahead of CA1 and PFC theta sequences differs during outbound versus inbound navigation

(A and **B)** Theta sequences representing past, current, and future locations on outbound (OUT) and inbound (IN) trajectories in **(A)** CA1 and **(B)** PFC. Each plot shows the averaged Bayesian reconstruction of all forward candidate theta sequences (sequence score $r > 0$), replicated over two theta cycles for visualization, relative to current position ($y = 0$; $y > 0$: ahead, or future location; $y < 0$: behind, or past location). Color bar: posterior probability. Arrowheaded line: animal's running direction.

(C and **D)** Distance index in **(C)** CA1 and **(D)** PFC across 8 sessions (E1-E8), compared the posterior probabilities on future versus past locations (< 0, biased to past; > 0, biased to future). 1st half of theta phases (light circles): -π to 0; 2nd half of theta phases (dark circles): 0 to π. Error bars: 95% CIs.

(E and **F)** Distributions for start and end of reconstructed trajectories relative to actual position ($x = 0$) of all significant forward theta sequences in **(E)** CA1 and **(F)** PFC. *Top*: Histograms show the distributions across all 8 sessions (dashed vertical lines: median values). *Bottom*: Averaged trajectory start (light circles) and end (dark circles) positions in individual sessions. ****p < 1e-4, **p = 0.007, Kolmogorov-Smirnov test.

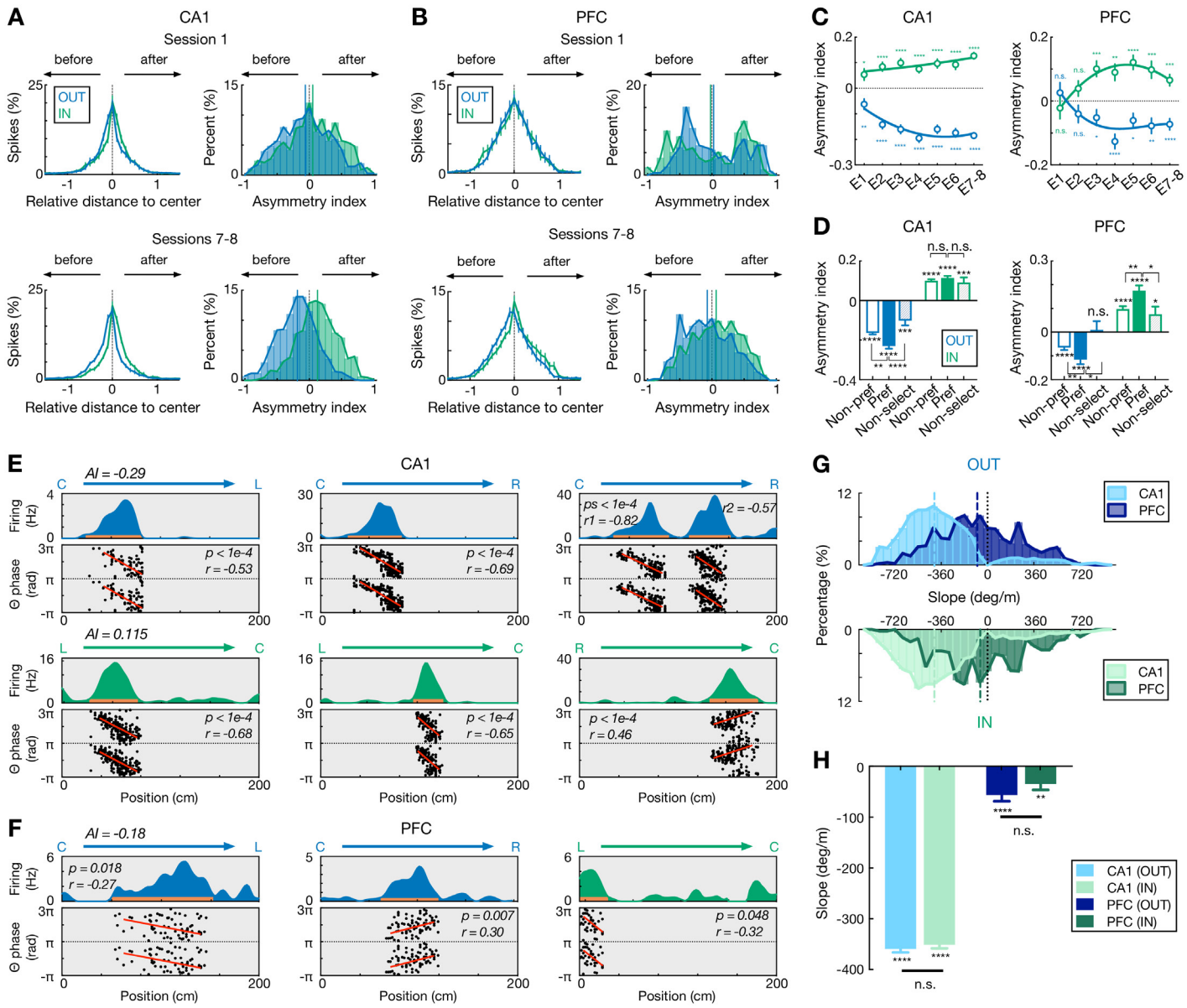

Figure 4. Comparisons of spatial-field asymmetry and theta phase precession during outbound versus inbound navigation in CA1 and PFC

(A and **B)** Spatial-field asymmetry during Session 1 (*top*) and Sessions 7-8 (*bottom*) in **(A)** CA1 and **(B)** PFC. Blue: outbound fields (OUT); Green: inbound fields (IN). *Left*: Averaged firing rate relative to field center (x = 0) across all cells in the given sessions (error bars: SEMs). *Right*: Distributions of spatial-field asymmetry index (colored vertical lines: mean values). See also single-field examples in **(E)** and **(F)**. **(C)** Spatial-field asymmetry index across sessions (****p < 1e-4, ***p < 0.001, **p < 0.01, *p < 0.05, n.s. p > 0.05, signed-rank tests compared to 0). Lines are derived from polynomial fits.

(D) Trajectory-selective cells exhibit highly asymmetric fields on the preferred (Pref) trajectory compared to the non-preferred trajectory (Non-pref). Non-select: non-selective cells. *P*-values for each condition derived from signed-rank tests compared to 0; *p*-values across conditions derived from rank-sum tests (****$p < 1e-4$, ***$p < 0.001$, **$p < 0.01$, *$p < 0.05$, n.s. $p > 0.05$).

(E and **F)** Single-cell examples of theta phase precession in **(E)** CA1 and **(F)** PFC for outbound (blue) and inbound (green) trajectories. For each example, linearized firing fields are shown on the *top* (trajectory type denoted above); spike theta phases against positions (i.e., phase precession) within individual spatial fields (indicated by an orange bar on the firing-field plot) are shown on the *bottom* (phases are plotted twice for better visibility; red lines represent linear-circular regression lines; linear-circular correlation coefficient *r* and its *p*-value denoted). AI: spatial-field asymmetry index.

(G) Distributions of phase precession slopes for outbound and inbound fields. *Top*: outbound; *bottom*: inbound. Vertical lines: median values.

(H) Phase precession slopes were similar during outbound versus inbound navigation in CA1 and PFC (n.s., *p's* > 0.99, Kruskal-Wallis test with Dunn's *post hoc*), and biased toward negative values (****$p < 1e-4$, **$p = 0.0012$, signed-rank tests compared to 0). This bias is stronger in CA1 than PFC (*p's* < 1e-4, Kruskal-Wallis test with Dunn's *post hoc*). Only fields with significant phase precession (see **METHODS**) are shown (mean ± SEM = 46.0 ± 2.8% in CA1, 11.2 ± 1.7% in PFC for inbound, and 48.8 ± 3.3% in CA1, 10.3 ± 1.2% in PFC for outbound).

Error bars: SEMs.

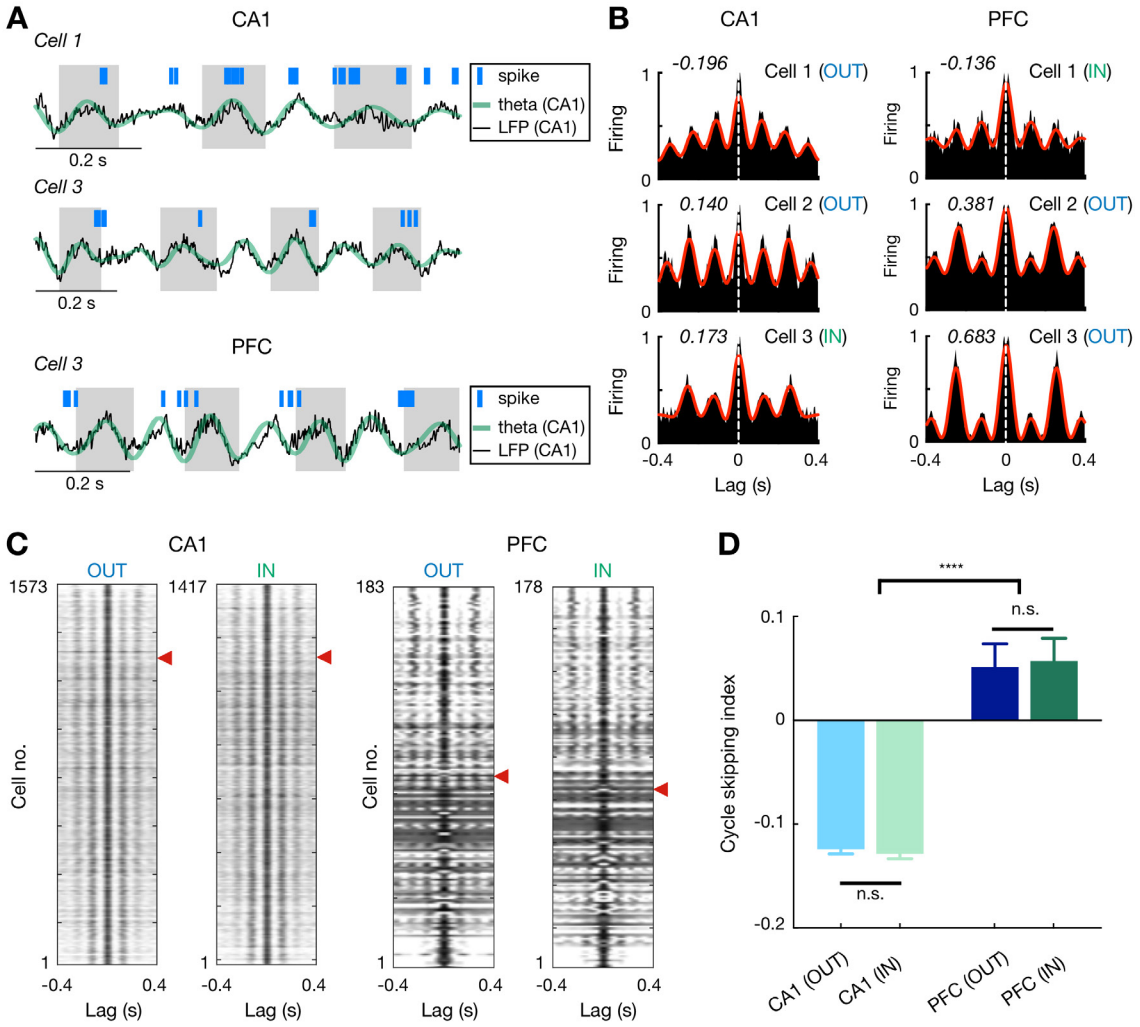

Figure 5. Theta cycle skipping in CA1 and PFC

(A) Spike rasters of example cells during CA1 theta oscillations. *Top*: a non-skipping (firing on adjacent cycles) CA1 cell; *Middle*: a cycle-skipping (firing on every other cycles) CA1 cell; *Bottom*: a cycle-skipping PFC cell. Black and green lines: broadband and theta-filtered LFPs from CA1 reference tetrode, respectively.

(B) Auto-correlograms (ACGs) of three example single cells in CA1 (*left*) and PFC (*right*). Each plot is of data from a single type of maze travel (outbound or inbound; travel type denoted). For each plot, cycle skipping index (CSI) is denoted on the upper left corner (CSI < 0: firing on adjacent cycles; CSI > 0: cycle skipping), and cell number with maze travel type (IN or OUT) matched to **(A)** is denoted on the upper right

corner. Red line: low-passed (1-10 Hz) ACG to measure CSI (see **METHODS**). Note that cells on the bottom two rows exhibit cycle skipping, with CSI > 0.

(C) ACGs of all theta-modulated cells in CA1 (*left*) and PFC (*right*) ordered by their CSIs (high to low from top to bottom). Red arrowheads indicate division between cells with CSI > 0 (above) vs. < 0 (below). Each row represents a single cell with one type of maze pass (outbound or inbound). Only cells with theta-modulated ACGs are shown (see **METHODS**). Note that the proportion of theta-cycle skipping cells in CA1 is consistent with that reported in previous studies (Kay et al., 2020).

(D) CSI of theta-modulated cells didn't differ significantly on outbound versus inbound trajectories for each region (n.s., *p's* > 0.99 for CA1 and PFC), but was larger in PFC than CA1 (****p < 1e-4, Kruskal-Wallis tests with Dunn's *post hoc*). Data are presented as mean and SEMs.

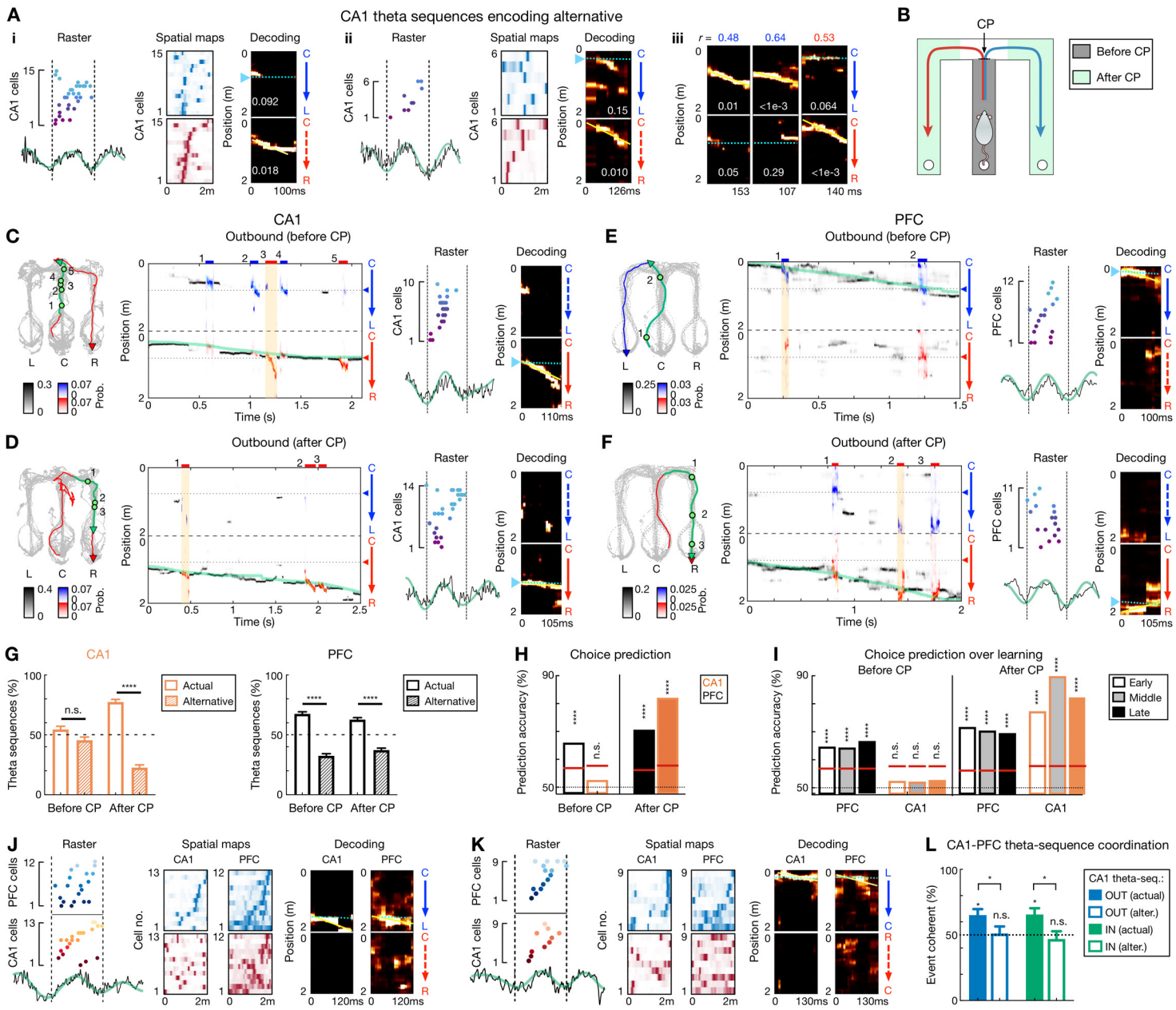

Figure 6. Theta-sequence representations of behavioral choices in CA1 and PFC

(A) Single-event examples of CA1 theta sequences encoding alternative. Two detailed example sequences are shown in **(Ai)** and **(Aii)** (presented as in **Figure 2A**). Three more examples with decoding plots only are shown in **(Aiii)** (presented as in **Figure 2C**).

(B) Diagram showing two task segments of a behavioral trial (or trajectory): before choice point (CP; gray shading), and after CP (green shadings).

(C-F) Four decoding examples for before and after CP during outbound navigation in **(C** and **D)** CA1 and **(E** and **F)** PFC. *Left*: Animal's behavior. Green line: the trajectory pass shown on the *middle*; Blue/red arrowheaded line: currently taken trajectory. Green circles: locations where theta-sequence events occurred (numbered corresponding to *middle*). *Middle*: Decoding plots. Data are presented as in **Figures 1F** and **1G** (bin = 120 ms), except that whenever a theta sequence was detected, the decoding was performed on the theta timescale (bin = 30 ms) and color-coded by trajectory type for clarity (red or blue: R-side or L-side trajectory; bars above show decoded identity and timing of each event). Note that at both timescales, summed probability of each column across two trajectory types is 1. Yellow shading: example event with detailed view shown on the *right*. Prob.: probability.

(G) Percent of theta sequences representing actual or alternative choice before and after CP in CA1 (*left*) and PFC (*right*) (****p < 1e-4, n.s. p > 0.05, session-by-session rank-sum paired tests). Error bars: SEMs.

(H) Trial-by-trial theta-sequence prediction of choice (****p < 0.0001, n.s., p > 0.05, trial-label permutation tests). Red horizontal lines: chance levels (i.e., 95% CIs of shuffled data) calculated by permutation tests.

(I) Theta-sequence prediction persists over sessions. Early: Sessions 1-3; Middle: Sessions 4-5; Late: Sessions 6-8. Data are presented as in **(H)**. Only correct trials are shown in **(H)** and **(I)**.

(J-L) Coherent CA1-PFC theta sequences biased to actual choice. **(J** and **K)** Two examples of coherent CA1-PFC theta sequences. **(L)** Percent of coordinated CA1-PFC theta sequences coherently representing actual vs. alternative choices (for each condition from left to right: p = 0.0312, 0.94, 0.0312, 0.48, signed-rank test compared to 50%; for comparisons between two conditions from left to right, p = 0.0312 and 0.0469, rank-sum tests). OUT: outbound; IN: inbound. Alter.: alternative choice. Error bars: SEMs.

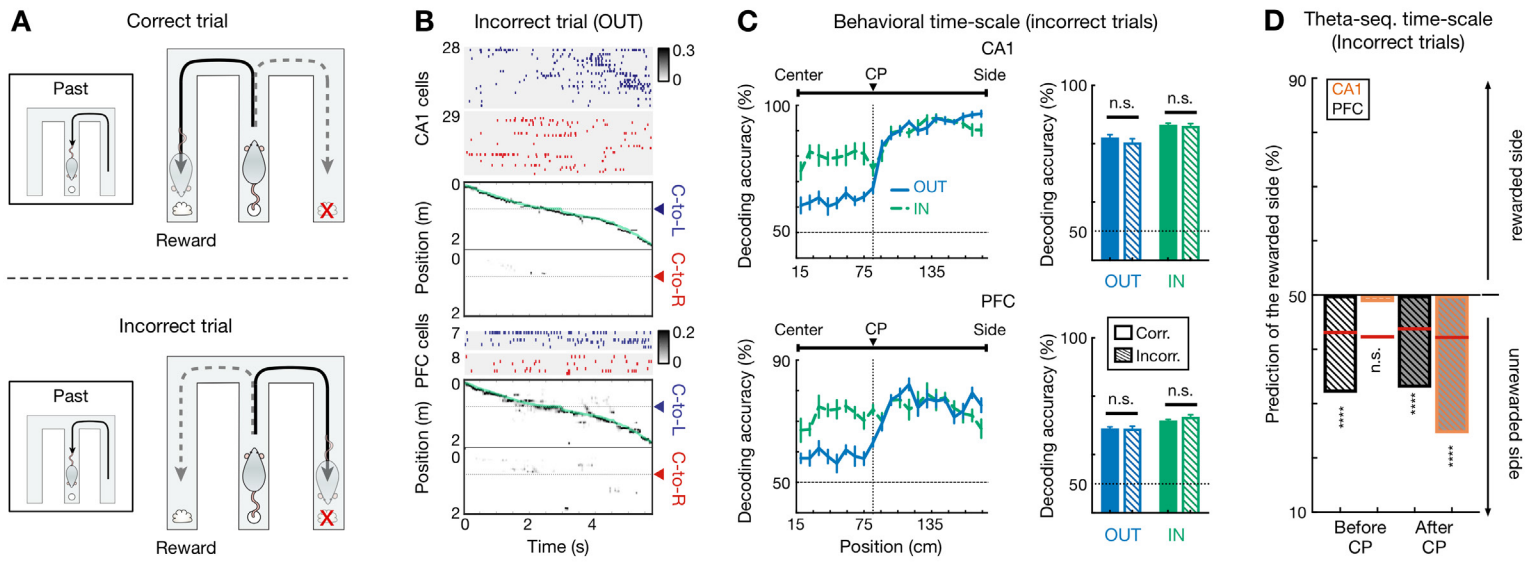

Figure 7. Choice representations of behavioral and theta sequences in CA1 and PFC were maintained during incorrect trials

(A) Illustration of a set of correct (*top*) and incorrect (*bottom*) trials. For incorrect trial, the actual choice is the unrewarded side.

(B and **C)** Behavioral sequences encoded current choice during incorrect trials. **(B)** Rasters and population decoding during an incorrect outbound trial. Data are taken from the same session and animal and presented as in **Figure 1F**. **(C)** Choice decoding accuracy during incorrect trials is not significantly different from that during correct trials in CA1 (n.s., $p > 0.99$ for outbound, = 0.67 for inbound) and PFC (n.s., $p > 0.99$ for outbound, = 0.11 for inbound; Friedman tests with Dunn's *post hoc*). Corr.: correct trials; Incorr.: incorrect trials. Inbound trials for the incorrect condition were taken from the one right before an incorrect outbound trial (i.e., "Past" trial of the diagram shown in **A**).

(D) Choice representations of theta sequences were similar during incorrect and correct (see **Figure 6H**) trials. Black bars are for PFC theta sequences, orange bars are for CA1.

558 **METHODS**

559 **Subjects**

560 Nine adult male Long-Evans rats (450-550 g, 4-6 months) were used in this study. All procedures were
561 approved by the Institutional Animal Care and Use Committee at the Brandeis University and conformed to
562 US National Institutes of Health guidelines. Data from six subjects have been reported in an earlier study
563 (Shin et al., 2019).

564
565 **Animal pre-training**

566 Animals were habituated to daily handling for several weeks before training. After habituation, animals were
567 food deprived to 85-90% of their *ad libitum* weight, and pre-trained to run on a linear track (~1-m long) for
568 rewards (sweetened evaporated milk), and habituated to an high-walled, opaque sleep box (~30 × 30 cm)
569 as described previously (Jadhav et al., 2012; Jadhav et al., 2016; Tang et al., 2017). After the pre-training,
570 animals were surgically implanted with a multi-tetrode drive.

571

572 **Surgical implantation**

573 Surgical implantation procedures were as previously described (Jadhav et al., 2012; Jadhav et al., 2016;
574 Shin et al., 2019; Tang et al., 2017). Eight animals were implanted with a multi-tetrode drive containing 32
575 independently moveable tetrodes targeting right dorsal hippocampal region CA1 (-3.6 mm AP and 2.2 mm
576 ML) and right PFC (+3.0 mm AP and 0.7 mm ML) (16 tetrodes in CA1 and 16 in PFC for 4 animals; 13 in
577 CA1 and 19 in PFC for 3 animals; 15 in CA1 and 17 in PFC for 1 animal). One animal was implanted with
578 a multi-tetrode drive containing 64 independently moveable tetrodes targeting the bilateral CA1 of dorsal
579 hippocampus (-3.6 mm AP and ±2.2 mm ML; **Figure S1A**, *left*) and PFC (+3.0 mm AP and ±0.7 mm ML;
580 **Figure S1B**, *left*) (30 tetrodes in CA1 and 34 tetrodes in PFC). On the days following surgery, hippocampal
581 tetrodes were gradually advanced to the desired depths with characteristic EEG patterns (sharp wave
582 polarity, theta modulation) and neural firing patterns as previously described (Jadhav et al., 2012; Jadhav
583 et al., 2016; Shin et al., 2019; Tang et al., 2017). One tetrode in corpus callosum served as hippocampal
584 reference (CA1 REF), and another tetrode in overlying cortical regions with no spiking signal served as
585 prefrontal reference (PFC REF). The reference tetrodes reported voltage relative to a ground (GND) screw

installed in skull overlying cerebellum. Electrodes were not moved at least 4 hours before and during the recording day.

Behavioral task

Following recovery from surgical implantation (~7-8 days), animals were food-deprived and again pre-trained on a linear track for at least two days before the W-track sessions started. During the recording day, animals were introduced to the novel W-track (**Figure 1A**; ~80 × 80 cm with ~7-cm wide tracks) for the first time, and learned the task rules over 8 behavioral sessions (or epochs, denoted as E1-E8; **Figure 1B**). Each behavioral session lasted 15-20 mins and was interleaved with 20-30 min rest sessions in the sleep box (total recording duration ≅ 6 hours within a single day) (Shin et al., 2019). On the W-maze, animals were rewarded for performing a hippocampus- (Fernandez-Ruiz et al., 2019; Jadhav et al., 2012; Kim and Frank, 2009) and prefrontal-dependent (Maharjan et al., 2018) continuous alternation task: returning to the center well after visits to either side well (left or right well; inbound trajectories), and choosing the opposite side well from the previously visited side well when starting from the center well (outbound trajectories). Rewards were automatically delivered in the reward wells (left well: L; right well: R; center well: C) triggered by crossing of an infrared beam by the animal's nose. Therefore, animals performed four types of trajectories during correct behavioral sequences in this task: center-to-left (C-to-L), left-to-center (L-to-C), center-to-right (C-to-R), and right-to-center (R-to-C). Among these trajectory types, C-to-L and C-to-R are outbound trajectories, while L-to-C and R-to-C are inbound trajectories. When animals were on the center stem, the two inbound trajectories thus represented possible past paths (one actual, and one alternative; **Figure 1A**, *left*), and the two outbound trajectories represented possible future paths (**Figure 1A**, *right*). The learning curves were estimated using a state-space model (**Figure 1B**) (Jadhav et al., 2012; Shin et al., 2019; Smith et al., 2004).

Behavioral analysis

Locomotor periods, or theta states, were defined as periods with running speed > 5 cm/s, whereas immobility was defined as periods with speed ≤ 4 cm/s. The animal's arrival and departure at a reward well was detected by an infrared beam triggered at the well. The well entry was further refined as the first time

point when the speed fell below 4 cm/s before the arrival trigger, whereas the well exit was defined as the first time point when the speed rose above 4 cm/s after the departure trigger (Shin et al., 2019). The time spent at a reward well (i.e., immobility period at well) was defined as the period between well entry and exit. Only SWRs occurring during immobility periods at reward wells were analyzed in this study (see also *SWR detection*). The center stem of the W-maze was defined as the set of linear positions (see *Spatial fields and linearization*) between the center well and the center junction (i.e., choice point, CP). For a given behavioral trajectory, the before-CP period was defined as the time spent at the center stem, and the after-CP period was defined as the time spent at locations between 10 cm away from the center stem and the side well (**Figures 6** and **S4-S5**). Therefore, for outbound trajectories, before-CP periods began when animals exited the center well and ended when animals reached the choice point (**Figure 6**), and for inbound trajectories, before-CP periods began when animals entered the choice point from the side arm and ended when animals entered the center well (**Figures S4-S5**).

Neural recordings

Data were collected using a SpikeGadgets data acquisition system (SpikeGadgets LLC) (Shin et al., 2019; Tang et al., 2017). Spike data were sampled at 30 kHz and bandpass filtered between 600 Hz and 6 kHz. LFPs were sampled at 1.5 kHz and bandpass filtered between 0.5 Hz and 400 Hz. The animal's position and running speed were recorded with an overhead color CCD camera (30 fps) and tracked by color LEDs affixed to the headstage. Single units were identified by manual clustering based on peak and trough amplitude, principal components, and spike width using custom software (MatClust, M. P. Karlsson) as previously described (Jadhav et al., 2016; Shin et al., 2019; Tang et al., 2017). Only well isolated neurons with stable spiking waveforms were included (Shin et al., 2019).

Histology

Following the conclusion of the experiments, micro-lesions were made through each electrode tip to mark recording locations (Shin et al., 2019). After 12-24 hours, animals were euthanized (Beuthanasia) and intracardially perfused with 4% formaldehyde using approved procedures. Brains were fixed for 24 hours, cryoprotected (30% sucrose in 4% formaldehyde), and stored at 4 °C. The recording sites were determined

642 from *post hoc* Nissl-stained coronal brain sections based on *The Rat Brain in Stereotaxic Coordinates*
643 (Paxinos and Watson, 2004) (**Figures S1A** and **S1B**).
644
645 **Cell inclusion**
646 Units included in analyses fired at least 100 spikes in a given session. Putative interneurons were identified
647 and excluded based on spike width and firing rate criterion as previously described (Jadhav et al., 2012;
648 Jadhav et al., 2016). Peak rate for each unit was defined as the maximum rate across all spatial bins in the
649 linearized spatial field (see *Spatial fields and linearization*). A peak rate ≥ 3 Hz was required for a cell to be
650 considered as a place cell.
651
652 **Spatial fields and linearization**
653 Spatial fields were calculated only during locomotor periods (> 5 cm/s; all SWR times excluded) at positions
654 with sufficient occupancy (> 20 ms). To construct the 1D linearized spatial fields on different trajectory
655 types, animal's linear positions were first estimated by projecting its actual 2D positions onto pre-defined
656 idealized paths along the track, and further classified as belonging to one of the four trajectory types (Shin
657 et al., 2019; Tang et al., 2017). The linearized spatial fields were then calculated using spike counts and
658 occupancies in 2-cm bins of the linearized positions and smoothened with a Gaussian curve (4-cm SD).
659 We found all linearized positions along each trajectory type were sufficiently covered by the spatial fields
660 of CA1, as well as PFC, populations (Shin et al., 2019).
661
662 **Trajectory selective index**
663 To measure the trajectory selectivity of single cells, a trajectory selectivity index (*SI*) was calculated by
664 comparing the mean firing rates on the Left- (or L-) vs. Right- (or R-) side trajectories for outbound (C-to-L
665 vs. C-to-R) and inbound (L-to-C vs. R-to-C), respectively:

666 $$SI = \frac{FR_L - FR_R}{FR_L + FR_R},$$

667 where FR_L is the mean firing rate on the L-side trajectory, and FR_R is for the R-side trajectory. Only cells
668 that had at least one spatial field (peak firing rate ≥ 3 Hz) detected on either the L- or R-side trajectory were

669 considered, and the spatial fields in different sessions were analyzed separately. A cell with $|SI| > 0.4$ in
670 CA1, or $|SI| > 0.2$ in PFC was classified as trajectory-selective cells ($|SI| = 0.384 \pm 0.004$ and 0.154 ± 0.003
671 for all CA1 and PFC cells, respectively; mean ± SEM) (Kay et al., 2020). The trajectory type (L vs. R) with
672 highest firing rate was designated as the cell's preferred (Pref) trajectory, and the other type designated as
673 the non-preferred (Non-pref) trajectory.
674
675 **SWR detection**
676 Sharp-wave ripples (SWRs) were detected during immobility periods (≤ 4 cm/s) as described previously
677 (Jadhav et al., 2012; Jadhav et al., 2016; Shin et al., 2019; Tang et al., 2017). In brief, LFPs from CA1
678 tetrodes relative to the CA1 reference tetrode were filtered into the ripple band (150-250 Hz), and the
679 envelope of the ripple-filtered LFPs was determined using a Hilbert transform. SWRs were initially detected
680 as contiguous periods when the envelope stayed above 3 SD of the mean on at least one tetrode, and
681 further refined as times around the initially detected events during which the envelope exceeded the mean.
682 For replay and reactivation analysis, only SWRs with a duration ≥ 50 ms were included as in previous
683 studies (Pfeiffer and Foster, 2013; Shin et al., 2019).
684
685 **Theta phases and theta cycles**
686 Peaks and troughs of theta oscillations, as well as theta phases, were identified on the band-passed (6-12
687 Hz) LFPs from the CA1 reference tetrode (CA1 REF) (Jadhav et al., 2016; Lubenov and Siapas, 2009). To
688 precisely define a theta cycle for theta sequence detection, theta phase locking of each cell in CA1 was
689 calculated across locomotor periods (> 5 cm/s) in each session using the methods developed in previous
690 reports (Jadhav et al., 2016; Siapas et al., 2005). A phase histogram was then calculated by averaging
691 across all phase-locked CA1 cells (Rayleigh tests at $p < 0.05$) in each session, and the phase with minimum
692 cell firing was used to separate theta cycles in the given session (approximately valley-to-valley of
693 hippocampal REF theta, or peak-to-peak of hippocampal fissure theta) (Gupta et al., 2012).
694
695 **Theta phase precession**

696 Theta phase precession was examined in linearized spatial fields with a peak rate ≥ 3 Hz, and multiple
697 fields of a single cell were analyzed separately (e.g., **Figure 4E**, *top right*). For each firing peak of linearized
698 spatial fields detected (using MATLAB *findpeaks* function with a 20-cm minimal peak distance), a spatial
699 field was defined as contiguous positions with rate > 10% of the peak rate, and at least 8 cm large (**Figures**
700 **4E** and **4F**) (Schmidt et al., 2009). For spikes within each spatial field, phase precession was computed
701 using a circular-linear fit as previously described (*cl_corr* function in the *measure_phaseprec* toolbox;
702 *https://github.com/HoniSanders/measure_phaseprec*) (Kempter et al., 2012; Sanders et al., 2019). The
703 slope, correlation coefficient (*r*), and its *p*-value from the circular-linear regression were reported (**Figures**
704 **4E-4H**).
705
706 **Theta power and coherence**
707 Power spectra and coherograms were computed from the LFPs referenced to GND using multitaper
708 estimation methods from the Chronux toolbox (http://chronux.org; version 2.12) (Shin et al., 2019). We
709 obtained the SD and mean for each frequency across a given session, and normalized the power of that
710 frequency as a z-score (**Figure S6B**). Coherence between a pair of CA1 and PFC tetrodes was calculated
711 during locomotor periods (> 5 cm/s; locations within 15 cm of the reward well were excluded to prevent
712 contamination from SWR activity). Coherograms averaged over all available CA1-PFC tetrode pairs with
713 simultaneously recorded LFPs were shown in **Figures S6C** and **S6D**. Theta power and coherence were
714 measured as the mean power and coherence between 6-12 Hz, respectively.
715
716 **Spatial field asymmetry**
717 For cells showing significant phase precession (circular-linear regression at $p < 0.05$), we further analyzed
718 their spatial field asymmetry (**Figures 4A-4D**). Only fields with the highest peak rate of a single cell for each
719 trajectory type, and at least 20 cm large, were used. The spatial fields were then binned into 10% field
720 length relative to field center (Souza and Tort, 2017), and the asymmetry index (*AI*) was calculated as:
721

$$AI = \frac{A_R - A_L}{A_R + A_L},$$

where A_R denoted the area under the firing rate profile to the right of the field center (i.e., $x > 0$ in **Figures 4A** and **4B**), while A_L represented the same to the left of the field center (i.e., $x < 0$ in **Figures 4A** and **4B**). Therefore, a negative *AI* corresponds to a spatial field with an extended initial tail.

Theta cycle skipping

To quantify theta cycle skipping in single cells (**Figure 5**), we measured a cycle skipping index (CSI) on their auto-correlograms (ACGs). Data on different trajectory types were analyzed separately, and thus a single cell could contribute to more than one ACG (**Figures 5B-5D**). For each ACG, data was restricted to locomotor periods (> 5 cm/s) that lasted at least 1.5 s, and with at least total 100 spikes (Kay et al., 2020). Each ACG was first estimated as a histogram of nonzero lags across the interval ± 400 ms (bin = 10 ms; denoted as *ACG_raw*) (Brandon et al., 2013; Kay et al., 2020), and was further corrected for the triangular shape caused by finite duration data (Kay et al., 2020; Mizuseki et al., 2009):

$$ACG(t) = \frac{ACG_raw(t)}{1 - \frac{|t|}{T}},$$

where t is the time lag ($-T < t < T$), and T is the total duration of the spike train used to compute the ACG. The corrected ACG was then smoothed (Gaussian kernel, SD = 20 ms) and peak-normalized. To detect the theta-modulated peaks of ACGs, power spectra for ACGs were generated using FFT, and the relative theta power of an ACG was calculated by dividing its power in the theta band (6-10 Hz) by its total power in the 1-50 Hz range (Deshmukh et al., 2010). An ACG with relative theta power > 0.15 was considered theta-modulated. For all theta-modulated ACGs, the ACGs were band-pass filtered between 1 and 10 Hz (Deshmukh et al., 2010), and the amplitudes of the first and second theta peaks on the filtered ACG were then determined by finding a first peak (p_1) near $t = 0$ in the 90-200 ms window, and the second peak (p_2) near $t = 0$ in the 200-400 ms window, as described previously (Kay et al., 2020). The CSI was then determined as:

$$CSI = \frac{p_2 - p_1}{\max(p_1, p_2)},$$

The CSI ranges between −1 and 1, and higher values indicate more theta cycle skipping.

Sequence analysis

Sequence analysis here focused on three different ensemble sequences: behavioral sequences, theta sequences, and replay sequences (**Figure 1C**). To evaluate neural representations at the ensemble level, Bayesian decoding was implemented as previously described (Davidson et al., 2009; Shin et al., 2019; Tang et al., 2017; Zhang et al., 1998): a memoryless Bayesian decoder was built for different trajectory types (for outbound, C-to-L vs. C-to-R; for inbound, L-to-C vs. R-to-C) to estimate the probability of animals' position given the observed spikes (Bayesian reconstruction; or posterior probability matrix):

$$P(X,Tr|\mathbf{spikes}) = \frac{P(\mathbf{spikes}|X,Tr)P(X,Tr)}{P(\mathbf{spikes})},$$

where X is the set of all linear positions on the track for different trajectory types (i.e., Tr; $Tr \in \{L, R\}$, where L represents the L-side trajectory, R represents the R-side trajectory), and we assumed a uniform prior probability over X and Tr. Assuming that all N cells active in a sequence fired independently and followed a Poisson process:

$$P(\mathbf{spikes}|X,Tr) = \prod_{i=1}^{N} P(spikes_i|X,Tr) = \prod_{i=1}^{N} \frac{\left(\tau f_i\left(X,Tr\right)\right)^{spikes_i} e^{-\tau f_i(X,Tr)}}{spikes_i!},$$

where τ is the duration of the time window (see below), $f_i(X,Tr)$ is the expected firing rate of the i-th cell as a function of sampled location X and trajectory type Tr, and $spikes_i$ is the number of spikes of the i-th cell in a given time window. Therefore, the posterior probability matrix can be derived as follows:

$$P(X,Tr|\mathbf{spikes}) = C\left(\prod_{i=1}^{N} f_i\left(X,Tr\right)^{spikes_i}\right) e^{-\tau \sum_{i=1}^{N} f_i(X,Tr)},$$

where C is a normalization constant such that $\sum_{k=1}^{2}\sum_{j=1}^{D} P(x_j, tr_k|\mathbf{spikes}) = 1$ (x_j is the j-th position bin, D is the total length of the track, and tr_k is the k-th trajectory type; k = 1 or 2, representing L- or R-side trajectory, respectively).

Specifically, for behavioral sequences, the Bayesian decoder was used to decode animal's current location (x) and choice (tr) (**Figures 1F-1I** and **S1C-S1H**) as in previous studies (Shin et al., 2019). Data was restricted to locomotor periods (> 5 cm/s; locations within 15 cm of the reward well were excluded for decoding to prevent contamination from SWR activity), and binned into 120-ms bins (i.e., τ = 120 ms;

moving window with 60 ms overlap). For each time bin, the location and choice (i.e., trajectory type) with maximum decoded probability was compared to the actual position and choice of the animal in that bin (**Figures 1F-1I** and **S1C-S1H**). Decoding error of positions in this bin was determined as the linear distance between estimated position and actual position (**Figures S1C-S1H**), and the accuracy of animal's choices decoded was reported (**Figures 1H** and **1I**).

For theta sequences, we first defined candidate events as theta cycles with at least 5 cells active in a given brain region (CA1 or PFC). Only theta cycles with running speed > 10 cm/s, and a duration ranging from 100 to 200 ms were used (Feng et al., 2015). A time window of 20 ms (i.e., τ = 20 ms; moving window with 10 ms overlap) was used to examine theta sequence structure at a fast, compressed timescale. To identify sequential structure within a theta cycle, two measures were adapted from previous theta-sequence studies (Drieu et al., 2018; Farooq and Dragoi, 2019; Feng et al., 2015; Zheng et al., 2016). In the first method, a weighted correlation (Farooq and Dragoi, 2019; Feng et al., 2015), $r\left(x,t\middle|\mathbf{Pmat}\right)$, was calculated for the posterior probability matrix of each trajectory type (**Pmat**, $D \times T$, D is the total number of spatial bins, and T is the total number of temporal bins). The weighted means were computed across locations (x) and time (t) as:

$$E_X(x|\mathbf{Pmat}) = \frac{\sum_{i=1}^{T}\sum_{j=1}^{D} Pmat_{ij} x_j}{\sum_{i=1}^{T}\sum_{j=1}^{D} Pmat_{ij}},$$

$$E_T(t|\mathbf{Pmat}) = \frac{\sum_{j=1}^{D}\sum_{i=1}^{T} Pmat_{ij} t_i}{\sum_{j=1}^{D}\sum_{i=1}^{T} Pmat_{ij}},$$

and the weighted covariance, $covar\left(x,t\middle|\mathbf{Pmat}\right)$, was computed as:

$$covar(x,t|\mathbf{Pmat}) = \frac{\sum_{i=1}^{T}\sum_{j=1}^{D} Pmat_{ij}\left(x_j - E_X\left(x|\mathbf{Pmat}\right)\right)\left(t_i - E_T\left(t|\mathbf{Pmat}\right)\right)}{\sum_{i=1}^{T}\sum_{j=1}^{D} Pmat_{ij}},$$

where t_i is the i-th temporal bin, and x_j is the j-th spatial bin of the posterior probability matrix (**Pmat**). The weighted correlation was then calculated as:

$$r\left(x,t\middle|\mathbf{Pmat}\right)=\frac{covar\left(x,t\middle|\mathbf{Pmat}\right)}{\sqrt{covar\left(t,t\middle|\mathbf{Pmat}\right)covar\left(x,x\middle|\mathbf{Pmat}\right)}},$$

and the weighted correlation was reported as the sequence score (*r*).

In the second method, we measured whether the decoded positions in successive temporal bins of the posterior probability matrix were tightly arranged along an oblique line as previously reported (Davidson et al., 2009; Drieu et al., 2018; Feng et al., 2015). Briefly, the best-fit line of a theta sequence (e.g., yellow lines of the decoding plots in **Figures 2A-2F**) was determined by a fitted line that yielded maximum posterior probability in an 8-cm vicinity (*d*). For a given candidate line with a slope *v* and an intercept *ρ*, the average likelihood *R* that the decoded position is located within a distance *d* of that line is:

$$R\left(v,\rho\right)=\frac{1}{n}\sum_{k=0}^{n-1}P\left(\left|pos-vk\cdot\Delta t\right|\le d\right),$$

where *k* is the temporal bin of the posterior probability matrix, and Δt is the moving step of the decoding window (i.e., 10 ms). To determine the best-fit line for each theta sequence, we densely sampled the parameter space of *v* and *ρ* (*v* > 1 m/s to exclude stationary events) to find the value that maximized *R* (R_{max}, i.e., goodness-of-fit).

In order to assess the significance of theta sequences, we circularly shifted the space-bins of the posterior probability matrix (*n* = 1000 times) as described previously (Drieu et al., 2018; Farooq and Dragoi, 2019; Zheng et al., 2016), and calculated the weighted correlation and the goodness-of-fit from the shuffled data. A sequence was considered significant if it met two criteria: first, its sequence score (i.e., weighted correlation) exceeded the 97.5th percentile or was below the 2.5th percentile (for reverse sequences) of the shuffled distributions; and its goodness-of-fit (R_{max}) was higher than the 95th percentile of their shuffles. We considered the significant trajectory type as the decoded trajectory, and if more than one trajectory type were significant, the trajectory with the highest sequence score was considered as the decoded trajectory. For plotting purposes only, a moving window (30 ms, advanced in steps of 5 ms) was used for displaying theta sequences (**Figures 2** and **6** and **S2** and **S4**).

The detection of replay sequences has been described previously (Shin et al., 2019). Briefly, candidate replay events were defined as the SWR events during which ≥ 5 place cells fired. Each candidate event was then divided into 10-ms non-overlapping bins (i.e., *τ* = 10 ms), and decoded based on the Bayes'

rule described above. The assessment of significance for replay events was implemented by a Monte Carlo shuffle, in which the *R*-squared from linear regression on the temporal bins versus the locations of the posterior probability matrix was compared to the *R*-squared derived from the shuffled data (i.e., time shuffle, circularly shuffling temporal bins of the posterior probability matrix). A candidate event with an *R*-squared that exceeded the 95th percentile of their shuffles (i.e., $p < 0.05$) was considered as a replay event.

For SWR events with significant CA1 replay sequences detected, we further measured CA1-PFC reactivation during these events (**Figure S7**) as described previously (Shin et al., 2019). We only analyzed the events where ≥ 5 place cells and ≥ 5 PFC cells fired. Briefly, for an event with *N* CA1 and *M* PFC cells active, a ($N \times M$) synchronization matrix during RUN ($\mathbf{C_{RUN}}$) was calculated with each element ($C_{i,j}$) representing the Pearson correlation coefficient of the linearized spatial fields on a certain trajectory type (see *Spatial fields and linearization*) of the *i*-th CA1 cell and the *j*-th PFC cell. To measure the population synchronization pattern during the SWR, the spike trains during the SWR were divided into 10-ms bins and z transformed (Peyrache et al., 2009; Shin et al., 2019). The ($N \times M$) synchronization matrix during the SWR ($\mathbf{C_{SWR}}$) was then calculated with each element ($C_{i,j}$) representing the correlation of the spike trains of a CA1-PFC cell pair. Finally, the reactivation strength of this event for each trajectory type was measured as the correlation coefficient (*R*) between the population matrices, $\mathbf{C_{RUN}}$ and $\mathbf{C_{SWR}}$.

Theta-sequence prediction of behavioral choices

For theta-sequence prediction of behavioral choices (**Figures 6H** and **6I** and **S5C**), trial-by-trial classification analysis was performed using support vector machines (SVMs) through the *libsvm* library (version 3.12) (Chang and Lin, 2011). For each region (CA1 or PFC), two independent SVMs were trained for before-CP and after-CP periods. For each trial, the numbers of theta sequences representing the actual versus the alternative choice during a given period (before CP, or after CP) were used as a feature ($n = 2$) to predict the current choice (k = 2, L or R). All classifiers were *C*-SVMs with a radial basis function (Gaussian) kernel and trained on correct trials. Hyperparameter (C and γ; regularization weight and radial basis function width, respectively) selection was performed using a random search method with leave-one-out cross-validation to prevent overfitting. The selected hyperparameters were then used to report the leave-one-out cross-validation accuracy. The percentage of correctly inferred trials was computed across

all training/test trial combinations to give prediction accuracy. The significance of this prediction was determined by comparing to the distribution of shuffled data by randomly shuffling the trial labels (L or R), and this shuffled dataset was used to train a classifier in the same way as the actual dataset. A prediction accuracy based on the actual dataset that was higher than the 95th percentile of its shuffles ($p < 0.05$) was considered as significant. Only trials with at least one theta sequence for actual and alternative choices were used for prediction.

CA1-PFC reactivation prediction of correct and incorrect responses

For prediction of correct and incorrect responses with CA1-PFC reactivation (**Figures S7E** and **S7F**), SVMs were used similar to the theta-sequence prediction analysis (see above). Two independent SVMs were trained on forward and reverse replay events. For each trial, the averaged CA1-PFC reactivation strength for the actual versus the alternative trajectory across all reactivation events during immobility at the reward well *prior* to the trial was used as a feature ($n = 2$; **Figures S7A** and **S7B**) to predict correct versus incorrect responses ($k = 2$, correct or incorrect, regardless of which side arm that the animals choose (Singer et al., 2013)). The significance of this prediction was determined by comparing it to the distribution of shuffled data by randomly shuffling the trial labels (correct or incorrect), and this shuffled dataset was used to train a classifier in the same way as the actual dataset. Given the unbalanced nature of the dataset (a lot more correct trials than incorrect trials), we resampled the incorrect trials (with replacement) to match the correct trials, and used ROC analysis to measure the predictive power of the classifiers. The area under each ROC curve (AUC) was computed, and an AUC based on the actual dataset that was higher than the 95th percentile of its shuffles ($p < 0.05$) was considered as significant. Only trials with at least one reactivation event of the given type (forward or reverse) were used for prediction.

Statistical Analysis

Data analysis was performed using custom routines in MATLAB (MathWorks) and GraphPad Prism 8 (GraphPad Software). We used nonparametric and two-tailed tests for statistical comparisons throughout the paper, unless otherwise noted. We used Kruskal-Wallis or Friedman test for multiple comparisons, with *post hoc* analysis performed using a Dunn's test. $P < 0.05$ was considered the cutoff for statistical

875 significance. Unless otherwise noted, values and error bars in the text denote means ± SEMs. No statistical
876 methods were used to pre-determine sample sizes, but our sample sizes are similar to those generally
877 employed in the field.

REFERENCES

Baeg, E.H., Kim, Y.B., Huh, K., Mook-Jung, I., Kim, H.T., and Jung, M.W. (2003). Dynamics of population code for working memory in the prefrontal cortex. Neuron *40*, 177-188. doi: 10.1016/s0896-6273(03)00597-x

Bakhurin, K.I., Mac, V., Golshani, P., and Masmanidis, S.C. (2016). Temporal correlations among functionally specialized striatal neural ensembles in reward-conditioned mice. J Neurophysiol *115*, 1521-1532. doi: 10.1152/jn.01037.2015

Barnes, T.D., Kubota, Y., Hu, D., Jin, D.Z., and Graybiel, A.M. (2005). Activity of striatal neurons reflects dynamic encoding and recoding of procedural memories. Nature *437*, 1158-1161. doi: 10.1038/nature04053

Benchenane, K., Peyrache, A., Khamassi, M., Tierney, P.L., Gioanni, Y., Battaglia, F.P., and Wiener, S.I. (2010). Coherent theta oscillations and reorganization of spike timing in the hippocampal-prefrontal network upon learning. Neuron *66*, 921-936. doi: 10.1016/j.neuron.2010.05.013

Bernacchia, A., Seo, H., Lee, D., and Wang, X.J. (2011). A reservoir of time constants for memory traces in cortical neurons. Nat Neurosci *14*, 366-372. doi: 10.1038/nn.2752

Branco, T., Clark, B.A., and Hausser, M. (2010). Dendritic discrimination of temporal input sequences in cortical neurons. Science *329*, 1671-1675. doi: 10.1126/science.1189664

Brandon, M.P., Bogaard, A.R., Schultheiss, N.W., and Hasselmo, M.E. (2013). Segregation of cortical head direction cell assemblies on alternating theta cycles. Nat Neurosci *16*, 739-748. doi: 10.1038/nn.3383

Burgess, N., and O'Keefe, J. (2011). Models of place and grid cell firing and theta rhythmicity. Curr Opin Neurobiol *21*, 734-744. doi: 10.1016/j.conb.2011.07.002

Buzsaki, G., Peyrache, A., and Kubie, J. (2014). Emergence of Cognition from Action. Cold Spring Harb Symp Quant Biol *79*, 41-50. doi: 10.1101/sqb.2014.79.024679

Carr, M.F., Jadhav, S.P., and Frank, L.M. (2011). Hippocampal replay in the awake state: a potential substrate for memory consolidation and retrieval. Nat Neurosci *14*, 147-153. doi: 10.1038/nn.2732

Chang, C.-C., and Lin, C.-J. (2011). Libsvm. ACM Transactions on Intelligent Systems and Technology *2*, 1-27. doi: 10.1145/1961189.1961199

Crowe, D.A., Averbeck, B.B., and Chafee, M.V. (2010). Rapid sequences of population activity patterns dynamically encode task-critical spatial information in parietal cortex. J Neurosci *30*, 11640-11653. doi: 10.1523/JNEUROSCI.0954-10.2010

Davidson, T.J., Kloosterman, F., and Wilson, M.A. (2009). Hippocampal replay of extended experience. Neuron *63*, 497-507. doi: 10.1016/j.neuron.2009.07.027

Daw, N.D., and Dayan, P. (2014). The algorithmic anatomy of model-based evaluation. Philos Trans R Soc Lond B Biol Sci *369*. doi: 10.1098/rstb.2013.0478

Deshmukh, S.S., Yoganarasimha, D., Voicu, H., and Knierim, J.J. (2010). Theta modulation in the medial and the lateral entorhinal cortices. J Neurophysiol *104*, 994-1006. doi: 10.1152/jn.01141.2009

Dragoi, G., and Buzsaki, G. (2006). Temporal encoding of place sequences by hippocampal cell assemblies. Neuron *50*, 145-157. doi:

Drieu, C., Todorova, R., and Zugaro, M. (2018). Nested sequences of hippocampal assemblies during behavior support subsequent sleep replay. Science *362*, 675-679. doi: 10.1126/science.aat2952

Durstewitz, D., Vittoz, N.M., Floresco, S.B., and Seamans, J.K. (2010). Abrupt transitions between prefrontal neural ensemble states accompany behavioral transitions during rule learning. Neuron *66*, 438-448. doi: 10.1016/j.neuron.2010.03.029

Eichenbaum, H. (2017). Prefrontal-hippocampal interactions in episodic memory. Nat Rev Neurosci *18*, 547-558. doi: 10.1038/nrn.2017.74

Farooq, U., and Dragoi, G. (2019). Emergence of preconfigured and plastic time-compressed sequences in early postnatal development. Science *363*, 168-173. doi: 10.1126/science.aav0502

Feng, T., Silva, D., and Foster, D.J. (2015). Dissociation between the experience-dependent development of hippocampal theta sequences and single-trial phase precession. J Neurosci *35*, 4890-4902. doi: 10.1523/JNEUROSCI.2614-14.2015

Fernandez-Ruiz, A., Oliva, A., Fermino de Oliveira, E., Rocha-Almeida, F., Tingley, D., and Buzsaki, G. (2019). Long-duration hippocampal sharp wave ripples improve memory. Science *364*, 1082-1086. doi: 10.1126/science.aax0758

Fernandez-Ruiz, A., Oliva, A., Nagy, G.A., Maurer, A.P., Berenyi, A., and Buzsáki, G. (2017). Entorhinal–CA3 dual-input control of spike timing in the hippocampus by theta-gamma coupling. Neuron *93*, 1213-1226 e1215. doi: 10.1016/j.neuron.2017.02.017

Foster, D.J., and Wilson, M.A. (2007). Hippocampal theta sequences. Hippocampus *17*, 1093-1099. doi:

Frank, L.M., Brown, E.N., and Wilson, M. (2000). Trajectory encoding in the hippocampus and entorhinal cortex. Neuron *27*, 169-178. doi: 10.1016/s0896-6273(00)00018-0

Fujisawa, S., Amarasingham, A., Harrison, M.T., and Buzsaki, G. (2008). Behavior-dependent short-term assembly dynamics in the medial prefrontal cortex. Nat Neurosci *11*, 823-833. doi: 10.1038/nn.2134

Fuster, J. (2015). The Prefrontal Cortex (Academic Press).

Geisler, C., Robbe, D., Zugaro, M., Sirota, A., and Buzsaki, G. (2007). Hippocampal place cell assemblies are speed-controlled oscillators. Proc Natl Acad Sci U S A *104*, 8149-8154. doi:

Goldman-Rakic, P.S. (1995). Cellular basis of working memory. Neuron *14*, 477-485. doi: 10.1016/0896-6273(95)90304-6

Gordon, J.A. (2011). Oscillations and hippocampal-prefrontal synchrony. Curr Opin Neurobiol *21*, 486-491. doi: 10.1016/j.conb.2011.02.012

Gupta, A.S., van der Meer, M.A., Touretzky, D.S., and Redish, A.D. (2012). Segmentation of spatial experience by hippocampal theta sequences. Nat Neurosci *15*, 1032-1039. doi: 10.1038/nn.3138

Harvey, C.D., Coen, P., and Tank, D.W. (2012). Choice-specific sequences in parietal cortex during a virtual-navigation decision task. Nature *484*, 62-68. doi: 10.1038/nature10918

Hasz, B.M., and Redish, A.D. (2020). Spatial encoding in dorsomedial prefrontal cortex and hippocampus is related during deliberation. Hippocampus. doi: 10.1002/hipo.23250

Ito, H.T., Zhang, S.J., Witter, M.P., Moser, E.I., and Moser, M.B. (2015). A prefrontal-thalamo-hippocampal circuit for goal-directed spatial navigation. Nature *522*, 50-55. doi: 10.1038/nature14396

Jadhav, S.P., Kemere, C., German, P.W., and Frank, L.M. (2012). Awake hippocampal sharp-wave ripples support spatial memory. Science *336*, 1454-1458. doi: 10.1126/science.1217230

Jadhav, S.P., Rothschild, G., Roumis, D.K., and Frank, L.M. (2016). Coordinated excitation and inhibition of prefrontal ensembles during awake hippocampal sharp-wave ripple events. Neuron *90*, 113-127. doi: 10.1016/j.neuron.2016.02.010

Jezek, K., Henriksen, E.J., Treves, A., Moser, E.I., and Moser, M.B. (2011). Theta-paced flickering between place-cell maps in the hippocampus. Nature *478*, 246-249. doi: 10.1038/nature10439

Johnson, A., and Redish, A.D. (2007). Neural ensembles in CA3 transiently encode paths forward of the animal at a decision point. Journal of Neuroscience *27*, 12176-12189. doi:

Jones, M.W., and Wilson, M.A. (2005a). Phase precession of medial prefrontal cortical activity relative to the hippocampal theta rhythm. Hippocampus *15*, 867-873. doi:

Jones, M.W., and Wilson, M.A. (2005b). Theta rhythms coordinate hippocampal-prefrontal interactions in a spatial memory task. PLoSBiol *3*, e402. doi:

Karlsson, M.P., Tervo, D.G., and Karpova, A.Y. (2012). Network resets in medial prefrontal cortex mark the onset of behavioral uncertainty. Science *338*, 135-139. doi: 10.1126/science.1226518

Kay, K., Chung, J.E., Sosa, M., Schor, J.S., Karlsson, M.P., Larkin, M.C., Liu, D.F., and Frank, L.M. (2020). Constant Sub-second Cycling between Representations of Possible Futures in the Hippocampus. Cell *180*, 552-567 e525. doi: 10.1016/j.cell.2020.01.014

Kempter, R., Leibold, C., Buzsaki, G., Diba, K., and Schmidt, R. (2012). Quantifying circular-linear associations: hippocampal phase precession. J Neurosci Methods *207*, 113-124. doi: 10.1016/j.jneumeth.2012.03.007

Kim, S.M., and Frank, L.M. (2009). Hippocampal lesions impair rapid learning of a continuous spatial alternation task. PLoS One *4*, e5494. doi: 10.1371/journal.pone.0005494

Latimer, K.W., Yates, J.L., Meister, M.L., Huk, A.C., and Pillow, J.W. (2015). Single-trial spike trains in parietal cortex reveal discrete steps during decision-making. Science *349*, 184-187. doi: 10.1126/science.aaa4056

Lisman, J., and Redish, A.D. (2009). Prediction, sequences and the hippocampus. Philos Trans R Soc Lond B Biol Sci *364*, 1193-1201. doi: 10.1098/rstb.2008.0316

Lubenov, E.V., and Siapas, A.G. (2009). Hippocampal theta oscillations are travelling waves. Nature *459*, 534-539. doi:

Lundqvist, M., Rose, J., Herman, P., Brincat, S.L., Buschman, T.J., and Miller, E.K. (2016). Gamma and Beta Bursts Underlie Working Memory. Neuron *90*, 152-164. doi: 10.1016/j.neuron.2016.02.028

Maharjan, D.M., Dai, Y.Y., Glantz, E.H., and Jadhav, S.P. (2018). Disruption of dorsal hippocampal - prefrontal interactions using chemogenetic inactivation impairs spatial learning. Neurobiol Learn Mem *155*, 351-360. doi: 10.1016/j.nlm.2018.08.023

Mattar, M.G., and Daw, N.D. (2018). Prioritized memory access explains planning and hippocampal replay. Nat Neurosci *21*, 1609-1617. doi: 10.1038/s41593-018-0232-z

Maurer, A.P., and McNaughton, B.L. (2007). Network and intrinsic cellular mechanisms underlying theta phase precession of hippocampal neurons. Trends Neurosci *30*, 325-333. doi: 10.1016/j.tins.2007.05.002

Mehta, M.R., Lee, A.K., and Wilson, M.A. (2002). Role of experience and oscillations in transforming a rate code into a temporal code. Nature *417*, 741-746. doi:

Mehta, M.R., Quirk, M.C., and Wilson, M.A. (2000). Experience-dependent asymmetric shape of hippocampal receptive fields. Neuron *25*, 707-715. doi: 10.1016/s0896-6273(00)81072-7

Miller, E.K., Lundqvist, M., and Bastos, A.M. (2018). Working Memory 2.0. Neuron *100*, 463-475. doi: 10.1016/j.neuron.2018.09.023

Mizuseki, K., Sirota, A., Pastalkova, E., and Buzsaki, G. (2009). Theta oscillations provide temporal windows for local circuit computation in the entorhinal-hippocampal loop. Neuron *64*, 267-280. doi: 10.1016/j.neuron.2009.08.037

Papale, A.E., Zielinski, M.C., Frank, L.M., Jadhav, S.P., and Redish, A.D. (2016). Interplay between hippocampal sharp-wave-ripple events and vicarious trial and error behaviors in decision making. Neuron *92*, 975-982. doi: 10.1016/j.neuron.2016.10.028

Pastalkova, E., Itskov, V., Amarasingham, A., and Buzsaki, G. (2008). Internally generated cell assembly sequences in the rat hippocampus. Science *321*, 1322-1327. doi: 10.1126/science.1159775

Paxinos, G., and Watson, C. (2004). The Rat Brain in Stereotaxic Coordinates (Academic Press).

Petersen, P.C., and Buzsaki, G. (2020). Cooling of Medial Septum Reveals Theta Phase Lag Coordination of Hippocampal Cell Assemblies. Neuron *107*, 731-744 e733. doi: 10.1016/j.neuron.2020.05.023

Peyrache, A., Khamassi, M., Benchenane, K., Wiener, S.I., and Battaglia, F.P. (2009). Replay of rule-learning related neural patterns in the prefrontal cortex during sleep. Nat Neurosci *12*, 919-926. doi: 10.1038/nn.2337

Pezzulo, G., Donnarumma, F., Maisto, D., and Stoianov, I. (2019). Planning at decision time and in the background during spatial navigation. Current opinion in behavioral sciences *29*, 69-76. doi: 10.1016/j.cobeha.2019.04.009

Pezzulo, G., van der Meer, M.A., Lansink, C.S., and Pennartz, C.M. (2014). Internally generated sequences in learning and executing goal-directed behavior. Trends Cogn Sci *18*, 647-657. doi: 10.1016/j.tics.2014.06.011

Pfeiffer, B.E., and Foster, D.J. (2013). Hippocampal place-cell sequences depict future paths to remembered goals. Nature *497*, 74-79. doi: 10.1038/nature12112

Rich, E.L., and Wallis, J.D. (2016). Decoding subjective decisions from orbitofrontal cortex. Nat Neurosci *19*, 973-980. doi: 10.1038/nn.4320

Robbe, D., and Buzsaki, G. (2009). Alteration of theta timescale dynamics of hippocampal place cells by a cannabinoid is associated with memory impairment. J Neurosci *29*, 12597-12605. doi: 10.1523/JNEUROSCI.2407-09.2009

Sadacca, B.F., Mukherjee, N., Vladusich, T., Li, J.X., Katz, D.B., and Miller, P. (2016). The Behavioral Relevance of Cortical Neural Ensemble Responses Emerges Suddenly. J Neurosci *36*, 655-669. doi: 10.1523/JNEUROSCI.2265-15.2016

Sanders, H., Ji, D., Sasaki, T., Leutgeb, J.K., Wilson, M.A., and Lisman, J.E. (2019). Temporal coding and rate remapping: Representation of nonspatial information in the hippocampus. Hippocampus *29*, 111-127. doi: 10.1002/hipo.23020

Schmidt, B., Duin, A.A., and Redish, A.D. (2019). Disrupting the medial prefrontal cortex alters hippocampal sequences during deliberative decision making. J Neurophysiol *121*, 1981-2000. doi: 10.1152/jn.00793.2018

Schmidt, R., Diba, K., Leibold, C., Schmitz, D., Buzsaki, G., and Kempter, R. (2009). Single-trial phase precession in the hippocampus. Journal of Neuroscience *29*, 13232-13241. doi:

Shin, J.D., Tang, W., and Jadhav, S.P. (2019). Dynamics of Awake Hippocampal-Prefrontal Replay for Spatial Learning and Memory-Guided Decision Making. Neuron *104*, 1110-1125 e1117. doi: 10.1016/j.neuron.2019.09.012

Siapas, A.G., Lubenov, E.V., and Wilson, M.A. (2005). Prefrontal phase locking to hippocampal theta oscillations. Neuron *46*, 141-151. doi: 10.1016/j.neuron.2005.02.028

Sigurdsson, T., Stark, K.L., Karayiorgou, M., Gogos, J.A., and Gordon, J.A. (2010). Impaired hippocampal-prefrontal synchrony in a genetic mouse model of schizophrenia. Nature *464*, 763-767. doi: 10.1038/nature08855

Singer, A.C., Carr, M.F., Karlsson, M.P., and Frank, L.M. (2013). Hippocampal SWR activity predicts correct decisions during the initial learning of an alternation task. Neuron *77*, 1163-1173. doi: 10.1016/j.neuron.2013.01.027

Skaggs, W.E., McNaughton, B.L., Wilson, M.A., and Barnes, C.A. (1996). Theta phase precession in hippocampal neuronal populations and the compression of temporal sequences. Hippocampus *6*, 149-172. doi:

Smith, A.C., Frank, L.M., Wirth, S., Yanike, M., Hu, D., Kubota, Y., Graybiel, A.M., Suzuki, W.A., and Brown, E.N. (2004). Dynamic analysis of learning in behavioral experiments. J Neurosci *24*, 447-461. doi: 10.1523/JNEUROSCI.2908-03.2004

Souza, B.C., and Tort, A.B.L. (2017). Asymmetry of the temporal code for space by hippocampal place cells. Sci Rep *7*, 8507. doi: 10.1038/s41598-017-08609-3

Sreenivasan, K.K., and D'Esposito, M. (2019). The what, where and how of delay activity. Nat Rev Neurosci *20*, 466-481. doi: 10.1038/s41583-019-0176-7

Tang, W., and Jadhav, S.P. (2019). Sharp-wave ripples as a signature of hippocampal-prefrontal reactivation for memory during sleep and waking states. Neurobiol Learn Mem *160*, 11-20. doi: 10.1016/j.nlm.2018.01.002

Tang, W., Shin, J.D., Frank, L.M., and Jadhav, S.P. (2017). Hippocampal-prefrontal reactivation during learning is stronger in awake compared with sleep states. J Neurosci *37*, 11789-11805. doi: 10.1523/JNEUROSCI.2291-17.2017

Wang, M., Foster, D.J., and Pfeiffer, B.E. (2020). Alternating sequences of future and past behavior encoded within hippocampal theta oscillations. Science *370*, 247-250. doi: 10.1126/science.abb4151

Wikenheiser, A.M., and Redish, A.D. (2015). Hippocampal theta sequences reflect current goals. Nat Neurosci *18*, 289-294. doi:

Wood, E.R., Dudchenko, P.A., Robitsek, R.J., and Eichenbaum, H. (2000). Hippocampal neurons encode information about different types of memory episodes occurring in the same location. Neuron *27*, 623-633. doi: Doi 10.1016/S0896-6273(00)00071-4

Yu, J.Y., and Frank, L.M. (2015). Hippocampal-cortical interaction in decision making. Neurobiol Learn Mem *117*, 34-41. doi: 10.1016/j.nlm.2014.02.002

Zhang, K., Ginzburg, I., McNaughton, B.L., and Sejnowski, T.J. (1998). Interpreting neuronal population activity by reconstruction: unified framework with application to hippocampal place cells. J Neurophysiol *79*, 1017-1044. doi: 10.1152/jn.1998.79.2.1017

Zheng, C., Bieri, K.W., Hsiao, Y.T., and Colgin, L.L. (2016). Spatial Sequence Coding Differs during Slow and Fast Gamma Rhythms in the Hippocampus. Neuron *89*, 398-408. doi: 10.1016/j.neuron.2015.12.005

Zheng, C., Hwaun, E., and Colgin, L.L. (2020). Impairments in Hippocampal Place Cell Sequences during Errors in Spatial Memory. bioRxiv, 2020.2004.2020.051755. doi: 10.1101/2020.04.20.051755

Zielinski, M.C., Shin, J.D., and Jadhav, S.P. (2019). Coherent Coding of Spatial Position Mediated by Theta Oscillations in the Hippocampus and Prefrontal Cortex. J Neurosci *39*, 4550-4565. doi: 10.1523/JNEUROSCI.0106-19.2019

Zielinski, M.C., Tang, W., and Jadhav, S.P. (2020). The role of replay and theta sequences in mediating hippocampal-prefrontal interactions for memory and cognition. Hippocampus *30*, 60-72. doi: 10.1002/hipo.22821